NASA Technical Memorandum 101660

PREDICTION OF THE THERMAL ENVIRONMENTAL AND THERMAL RESPONSE OF SIMPLE PANELS EXPOSED TO RADIANT HEAT

TRAVIS L. TURNER
ROBERT L. ASH

OCTOBER 1989

NASA
National Aeronautics and
Space Administration

PREDICTION OF THE THERMAL ENVIRONMENT AND THERMAL RESPONSE OF SIMPLE PANELS EXPOSED TO RADIANT HEAT

Travis L. Turner
NASA Langley Research Center
Hampton, VA 23665

Robert L. Ash
Old Dominion University
Norfolk, VA 23508

ABSTRACT

A method of predicting the radiant heat flux distribution produced by a bank of tubular quartz heaters was applied to a radiant system consisting of a single unreflected lamp irradiating a flat metallic incident surface. In this manner, the method was experimentally verified for various radiant system parameter settings and used as a source of input for a finite element thermal analysis. Two finite element thermal analyses were applied to a thermal system consisting of a thin metallic panel exposed to radiant surface heating. A two-dimensional steady-state finite element thermal analysis algorithm, based on Galerkin's Method of Weighted Residuals (GFE), was formulated specifically for this problem and was used in comparison to the thermal analyzers of the Engineering Analysis Language (EAL). Both analyses allow conduction, convection, and radiation boundary conditions. Differences in the respective finite element formulation are discussed in terms of their accuracy and resulting comparison discrepancies. The thermal analyses are shown to perform well for the comparisons presented here with some important precautions about the various boundary condition models. A description of the experiment, corresponding analytical modelling, and resulting comparisons are presented.

SUMMARY

A method of predicting the radiant heat flux distribution produced by a bank of quartz heaters was experimentally verified in application to a radiant system involving a single unreflected quartz lamp irradiating a flat surface. The method is applicable to planar quartz radiant heating systems where the system reflector is either nonexistent or planar and the system geometry is well known. A specialized two-dimensional finite element code based on Galerkin's Method of Weighted Residuals (GFE) was developed for the prediction of the temperature distribution produced on simple panels by this radiant load. This method was compared with the thermal analyzers of the Engineering Analysis Language (EAL) and both methods were verified through comparison with experiment. The specialized GFE code is restricted to two-dimensional and steady-state analysis while EAL is not, but was found to be more reliable for the particular tests presented here. A description of the analytical modeling, the experimental set-up and procedure, and comparisons between analysis and experiment are presented.

INTRODUCTION

Aircraft operating in supersonic and hypersonic flight conditions are subjected to intense aerothermal and aeroacoustic loads. Aerothermal loading on these structures (i.e. boundary layer and jet plume heating) presents difficulty in the prediction of the elastic response. Problems including the temperature dependence of material properties, thermal stresses, thermal buckling, and snapthrough make accurate thermal modeling of the flight conditions imperative. An immediate goal is to establish representative thermal testing capabilities and to develop the necessary thermal environment and response prediction methods with sufficient accuracy.

Heat transfer in solids is a widely studied subject for which the theory is well developed and with the advancement of finite element solution methods, thermal analysis has received greatly extended practical application. However, this capability has rarely been experimentally verified.

The work presented here represents an effort to validate thermal load prediction and finite element thermal response analysis methods through comparison with experiments involving flat metallic panels exposed to radiant heat. These experiments are intended to be simple enough to minimize uncertainty, yet physically similar to more complex tests of a thermal-elastic nature. The goal is to develop proficeincy in analyzing complex thermal systems through stages of experimental comparison of increasing difficulty. The experiments include measurement of the radiant heat flux produced by a single unreflected quartz radiant heater and measurement of the resulting temperatures produced on thin metallic panels. It is apparent that two thermal analyses are required to describe these thermal testing conditions since the radiant thermal loading from the external source must be known before formulating a heat balance.

The radiant thermal load is defined through a differential analysis of the radiant system. This analysis provides a nondimensional distribution of radiant heat flux on a flat

1

incident surface which is then normalized by a factor involving the lamp power and system dimensions. This procedure is currently limited to a planar array of quartz radiant heaters irradiating a parallel planar surface at an arbitrary distance. Output may be generated at the central or nodal points of an arbitrary number of rectangular elements forming the incident surface. This output may then be used by a finite element thermal analyzer to determine the resulting response of the target structure.

Two finite element analyses were applied to accomplish this task in order to gain proficiency in finite element thermal analysis and to gain preliminary comparison capabilities. One analysis is a specialized finite element algorithm based on Galerkin's Method of Weighted Residuals (GFE), which was formulated for this work, and the other consists of the thermal analyzers of the Engineering Analysis Language (EAL). Both analyses use the radiant flux as input, but incorporate it in the analysis slightly differently. This difference in formulation, along with various others, will be discussed. Both analyses incorporate conductive, convective, and radiative boundary conditions. The comparisons are currently limited to the two dimensional steady-state heat transfer in thin metallic panels.

SYMBOLS AND ABBREVIATIONS

GFE	Galerkin Finite Element (finite element thermal analyzer)
EAL	Engineering Analysis Language (finite element analyzer)
$I_l(\hat{\Omega}, T)$	lamp surface radiant intensity, $W/m^2 \cdot sr$
I_0	uniform-assumption lamp surface radiant intensity, $W/m^2 \cdot sr$
$d\Omega$	solid angle subtended about radiation propagation direction, sr
Q_0	lamp radiant emissive power, W
$q_s(x,y)$	incident radiant heat flux, W/m^2
$T(x,y)$	surface temperature, K
$k_x(T), k_y(T)$	material thermal conductivities, $W/m \cdot K$
l	panel thickness, m
$\alpha(T)$	panel surface absorptivity
$\epsilon(T)$	panel surface emissivity
σ	Stefan-Boltzmann constant, $5.67 \times 10^{-8} \ W/m^2 \cdot K^4$
h	convective heat transfer coefficient, $W/m^2 \cdot K$
$h_\epsilon(x,y)$	effective radiation heat transfer coefficient, $W/m^2 \cdot K$
D^e	element surface area, m^2
S^e	element perimeter, m

2

$\vec{q}$	heat flux vector, W/m^2
$\hat{n}$	unit normal vector
C^0	finite element approximation ensuring continuity of field variable magnitude
∞	subscript indicating ambient quantity
e	superscript indicating element quantity
$^-$	superscript indicating approximate quantity

RADIANT THERMAL LOAD

The radiant thermal load may be defined for an arbitrary planar surface, given the radiant system geometry and power specifications . The radiant system considered in the formulation of this analysis is shown in figure 1. This figure represents the direct radiant energy transfer from a single lamp (of a multiple lamp system) to a flat incident surface. The resulting incident heat flux distribution from the entire lamp bank is the summation of the individual lamp contributions. The effect of incorporating a planar reflector in the radiant system may be analyzed by treating it as another incident surface with specular and diffuse reflectivity components. The analysis is based on the following assumptions. The receiving surface is black, the lamp filament emits symmetrically about its circumference and uniformly along its length, and the lamp diameter is small relative to the other system dimensions. The present work is further restricted to a single unreflected lamp irradiating a flat incident surface parallel to the lamp's axis. With these restrictions, figure 1 depicts the entire radiant system where only the directly incident radiant energy is considered.

A portion of the analysis given here was previously documented in an unpublished NASA contractor's report written by the second author of this paper under master contract agreement NAS1-9434, task order number 34. A new computer program was written to allow for generality in system configuration and to produce output on an element-nodal basis, consistent with the finite element thermal analysis method GFE. This computer program was tested for the simple radiant system discussed here.

The source of the radiant energy emitted from a quartz heater is a coiled tungsten filament. The radiant field produced by any differential element of this filament is a function of direction and element temperature. However, due to the complex scattering induced by the interaction of adjacent filament elements with each other and with the quartz tube, the emitted radiant intensity passing through a patch element on the surface of the quartz tube is assumed directionally independent. Furthermore, the lamp filament is assumed to operate at a uniform temperature allowing the lamp surface radiant intensity to be treated as a constant, designated by I_0.

Referring to figure 2, consider a hemisphere of radius r centered at the lamp surface element dA_l (patch element) such that its flat surface coincides with a plane tangent to dA_l and the hemisphere extends in the direction of $\hat{n}_l$. Let dA_n be the projection of dA_l onto

the hemisphere surface at the location of the incident surface element dA_s. The intensity of the emitted radiation is defined to be the amount of radiant energy transmitted per unit projected area, per unit solid angle about the propagation direction, and per unit time [1,2]. With this definition, the radiant intensity may be equated as

$$I_l(\hat{\Omega}, T) = \frac{dQ_n/dA_n}{d\Omega} \tag{1}$$

where I_l is the radiant intensity leaving the lamp surface element, dQ is the heating rate induced on the incident surface element, and $d\Omega$ is the solid angle around the direction of propagation. With the above assumptions concerning the radiant energy emitted by the lamp filament, the lamp surface radiant intensity in equation (1) may be replaced by the constant I_0. The various terms in equation (1) are related to the geometric quantities in figure (1) as follows

$$dA_n = dA_l \cos \theta_l$$
$$d\Omega = \sin \theta_l \, d\theta_l d\gamma \tag{2}$$
$$= \frac{dA_n}{r^2}$$

where r is the distance between the lamp surface element and the incident surface element, θ_l is the angle between the direction of r and the unit normal to dA_l, and γ is the polar angle measured in the plane of dA_l from a convenient datum. With these relations the heating rate generated on the differential area dA_n is equated to the appropriate quantities as

$$dQ_n = I_0 dA_l \cos \theta_l \sin \theta_l \, d\theta_l d\gamma \tag{3}$$

The radiant energy emitted by dA_l in all directions in the hemispherical space is then obtained from

$$Q_n = dA_l \int_0^{2\pi} d\gamma \int_0^{\frac{\pi}{2}} d\theta_l \, I_0 \cos \theta_l \sin \theta_l \tag{4}$$

to give

$$Q_n = \pi I_0 dA_l$$
$$= \frac{\pi I_0 D}{2} d\phi dx' \tag{5}$$

This expression may in turn be integrated over the surface area of the lamp to obtain the entire emissive power of the lamp (denoted by Q_0) as a function of the lamp surface radiant intensity. This integration has the form

$$Q_0 = \frac{\pi I_0 D}{2} \int_0^L dx' \int_0^{2\pi} d\phi \tag{6}$$

which may be evaluated to give

$$I_0 = \frac{Q_0}{\pi^2 DL} \tag{7}$$

If we now consider the radiant intensity in the same direction and location as in equation (1), but impinging upon the incident surface element, the associated solid angle

4

would be evaluated according to the view of dA_s by an observer at dA_l. This altered solid angle would account for the inclined orientation of dA_s with respect to the propagation direction and is given by

$$d\Omega_{ls} = \frac{dA_s \cos\theta_s}{r^2} \tag{8}$$

Denoting the heating rate at the incident surface element by dQ_s, it may be related to the intensity directly from equation (1) as

$$
\begin{aligned}
dQ_s &= I_0 dA_n d\Omega_{ls} \\
&= \frac{I_0 \cos\theta_l \cos\theta_s dA_l dA_s}{r^2}
\end{aligned}
\tag{9}
$$

For simplification, the above quantities may be written in terms of measureable geometric dimensions as follows.

$$
\begin{aligned}
\cos\theta_l &= \frac{\hat{n}_l \cdot \vec{r}}{r} = \frac{(y\sin\phi + H\cos\phi)}{r} \\
\cos\theta_s &= \frac{-\hat{k}\cdot\vec{r}}{r} = \frac{H}{r} \\
dA_l &= \frac{D}{2}d\phi dx' \\
r &= [(x-x')^2 + y^2 + H^2]^{1/2}
\end{aligned}
\tag{10}
$$

In these relations ϕ is the lamp circumference angle measured from the negative z-axis, D is the lamp diameter, L is the lamp filament lighted length, H is the perpendicular distance from the lamp axis to the incident surface, x and y are the spatial coordinates of dA_s, and x' is the axial coordinate of dA_l measured from the center of the lighted filament length. The radiant energy per unit area (flux) incident to dA_s due to the emission from the entire lamp is designated by q_s and is evaluated by integrating the effects of the differential lamp element (dA_l) over the length of the lighted filament and the circumference of the quartz tube, resulting in the equation

$$q_s(x,y) = \frac{I_0 H D}{2}\int_{-\frac{L}{2}}^{\frac{L}{2}} dx' \int_{\phi_r-\frac{\pi}{2}}^{\phi_r+\frac{\pi}{2}} \frac{d\phi(y\sin\phi + H\cos\phi)}{[(x-x')^2 + y^2 + H^2]^2} \tag{11}$$

where ϕ_r is shown in figure 1. This angle locates the constant-y line passing through dA_s relative to the z-axis and is given by

$$\phi_r = \tan^{-1}\frac{y}{H} \tag{12}$$

Performing the integration in ϕ results in equation (13).

$$q_s(x,y) = I_0 H D \sqrt{y^2 + H^2}\int_{-\frac{L}{2}}^{\frac{L}{2}} \frac{dx'}{[(x-x')^2 + y^2 + H^2]^2} \tag{13}$$

5

This equation may be nondimensionalized through manipulating the equation in such a way as to produce the parameters $\bar{q}_s$, ξ, ξ', ζ, and γ, defined by

$$\bar{q}_s(\xi,\zeta) = \frac{q_s(x,y)H^2}{I_0 D L} \qquad \xi = \frac{x}{L} \qquad \xi' = \frac{x'}{L} \qquad \zeta = \frac{y}{H} \qquad \gamma = \frac{L}{H} \qquad (14)$$

resulting in an equivalent dimensionless equation for $\bar{q}_s$.

$$\bar{q}_s(\xi,\zeta) = \sqrt{\zeta^2 + 1} \int_{-\frac{1}{2}}^{\frac{1}{2}} \frac{d\xi'}{[\gamma^2(\xi - \xi')^2 + \zeta^2 + 1]^2} \qquad (15)$$

Integrating this equation results in the dimensionless incident distribution $\bar{q}_s(\xi,\zeta)$.

$$\bar{q}_s(\xi,\zeta) = \frac{1}{2(\zeta^2 + 1)} \left[\frac{\gamma(\xi + \frac{1}{2})(\zeta^2 + 1)^{\frac{1}{2}}}{\gamma^2(\xi + \frac{1}{2})^2 + \zeta^2 + 1} - \frac{\gamma(\xi - \frac{1}{2})(\zeta^2 + 1)^{\frac{1}{2}}}{\gamma^2(\xi - \frac{1}{2})^2 + \zeta^2 + 1} \right.$$
$$\left. + \tan^{-1} \frac{\gamma(\xi + \frac{1}{2})}{(\zeta^2 + 1)^{\frac{1}{2}}} - \tan^{-1} \frac{\gamma(\xi - \frac{1}{2})}{(\zeta^2 + 1)^{\frac{1}{2}}} \right] \qquad (16)$$

With the relation given in equation (7) and the expression in equation (14) relating q_s to $\bar{q}_s$, the incident radiant heat flux may be written as

$$q_s(x,y) = \frac{Q_0}{2\pi^2 H^2 \alpha^2} \left[\frac{\beta}{(1 + \beta^2)} - \frac{\xi}{(1 + \xi^2)} + \tan^{-1}\beta - \tan^{-1}\xi \right] \qquad (17)$$

where the dimensionless parameters are related to the system variables by

$$\alpha = \sqrt{\left(\frac{y}{H}\right)^2 + 1} \qquad \beta = \frac{\frac{x}{H} + \frac{L}{2H}}{\alpha} \qquad \xi = \frac{\frac{x}{H} - \frac{L}{2H}}{\alpha} \qquad (18)$$

From equation (17), it is easily seen that the incident radiant flux is scaled by the quantity $\frac{Q_0}{HL}$ (i.e. W/m^2). It is important to note however that the lamp power term Q_0 is not equivalent to the lamp rating since the system is not conservative.

The nonconservative energy conversion includes losses due to the emission of spectral wavelengths that are 'non-thermal', conduction from the lamp ends, and convection from the lamp surface. The 'apparent' power that a particular point on the incident surface experiences is also a function of system geometry due to the changes in loss parameters. Therefore, it was decided that theory and analysis should be forced to agree at a selected point. This was accomplished experimentally by recording a single flux measurement at a geometrically convenient location for each experimental parameter setting. This measurement was used in equation (17) to extract an apparent power. Once this parameter dependent apparent power is determined, the resulting distribution of radiant heat flux over the entire defined region, with an arbitrary mesh size, may be calculated via equation (17).

6

FINITE ELEMENT THERMAL ANALYSIS

Galerkin Finite Element Formulation

The formulation of the specialized finite element thermal analysis (GFE) allowed comparisons with EAL's thermal capabilities. This was instrumental in determining the applicability of both algorithms. The GFE formulation is based on the application of Galerkin's Method of Weighted Residuals to the equation governing the steady-state two-dimensional heat transfer in thin plates. The governing partial differential equation is formulated through a heat balance in a plate (figure 3) as seen in appendix A, and is given by

$$\left[\frac{\partial}{\partial x}\left(k_x \frac{\partial T}{\partial x}\right) + \frac{\partial}{\partial y}\left(k_y \frac{\partial T}{\partial y}\right) \right] t = h(T - T_\infty) + \epsilon\sigma(T^4 - T_\infty^4) - \alpha q_s \qquad (19)$$

where x and y are the spatial coordinates in the plane of the plate, k_x and k_y are the plate material thermal conductivities, t is the plate thickness, h is the convective heat transfer coefficient, ϵ is the plate surface emissivity, σ is Stefan-Boltzmann's constant, α is the plate surface absorptivity, q_s is the incident radiant thermal load from the quartz heaters, and T and T_∞ are the plate surface and surroundings temperatures respectively. The convective heat transfer coefficient (h) may have contributions from one or both sides and free and/or forced convection. This coefficient has an average value which is based on the flow field over the entire plate surface. The radiation exchange term may be multiplied by an integer of value 1 or 2 through considering the exchange from one or both sides of the plate (appendix A). The particular comparisons presented here limit the convective and radiative exchange to the upper surface of the plate by insulating the lower surface. The imperfectly insulated lower surface condition was handled by applying a resistive analogy with temperature dependent insulation thermal conductivity as explained in the Thermal Experiments section. The above defined variables form distinct heat transfer terms in equation (19) such as the conduction through the plate (left hand side of the equation), convective exchange with the surroundings, and the radiant exchange with the surroundings. Similar examples of a heat balance formulation may be found in heat transfer texts such as reference 1.

If an equivalent radiative heat transfer coefficient is defined as

$$h_\epsilon = \epsilon\sigma(T^2 + T_\infty^2)(T + T_\infty) \qquad (20)$$

equation (19) may be written with a combined heat transfer coefficient.

$$\left[\frac{\partial}{\partial x}\left(k_x \frac{\partial T}{\partial x}\right) + \frac{\partial}{\partial y}\left(k_y \frac{\partial T}{\partial y}\right) \right] t = (h + h_\epsilon)(T - T_\infty) - \alpha q_s \qquad (21)$$

The effective radiation heat transfer coefficient may be evaluated, on an elementally-averaged basis, with the system-averaged convective heat transfer coefficient before a solution to the governing equation is attempted. Therefore, an application of a direct iteration technique, as will be explained in the next section, was used. The solution to equation

(21) is quite cumbersome, especially for complicated geometry and boundary conditions, unless some simplification is introduced. One such simplification results from the use of the method of weighted residuals.

The method of weighted residuals is a common technique for solving differential equations for which a closed form solution is unknown. It may be applied to the entire solution domain of a governing equation as seen in appendix B. The method of weighted residuals is a solution technique where the functional dependence of the continuous field variable, in this case $T(x, y)$, is assumed and substituted into the governing equation. In all probability, the assumed functional variation will not solve the problem exactly, leaving a residual. The residual is then required to vanish in an averaged sense over the solution domain [3]. In application to this particular problem, the field variable is approximated by discrete values interrelated by some arbitrary functions. This may be accomplished through a weighted sum of the discrete values as in equation (22)

$$T \approx \bar{T} = \sum_{i=1}^{m} F_i T_i \tag{22}$$

where F_i are the arbitrary weighting functions, T_i are the discrete temperatures, and m is the number of discrete temperatures. The residual resulting from this approximation is then minimized through a weighted integration over the solution domain (appendix B). Galerkin's method consists of choosing integration weighting functions such that they are equivalent to the spatial weighting functions.

Thus far, this discussion has been concerned with the entire solution domain, however, this simplification should be equally applicable to any portion of this region. Referring to figure 4, the temperature distribution across a four-noded rectangular portion of this domain, or rectangular element, may be expressed in the form

$$T^e(x, y) \approx \bar{T}^e(x, y) = \lfloor N \rfloor \{T\}^e \tag{23}$$

where the superscript (e) designates the element-domain nature of the equation. Here the arbitrary functions have taken on the identity of element interpolation functions, where $\lfloor N \rfloor$ designates a row vector of these functions, and $\{T\}$ is a column vector of nodal temperatures. For this application, linear interpolation functions were chosen for simplicity and are sufficient since continuity of field variable (temperature) magnitude (C^0 continuity) is all that is required at element interfaces. Recognizing that a rectangular element with linear interpolation functions must have four nodes, the linear interpolation functions are written in the natural or local coordinates as

$$\{N\} = \begin{Bmatrix} N_1 \\ N_2 \\ N_3 \\ N_4 \end{Bmatrix} = \begin{Bmatrix} (1 - \frac{x}{a})(1 - \frac{y}{b}) \\ \frac{x}{a}(1 - \frac{y}{b}) \\ (\frac{x}{a})(\frac{y}{b}) \\ \frac{y}{b}(1 - \frac{x}{a}) \end{Bmatrix} \tag{24}$$

where a and b are the length and width of the element respectively.

8

Rewriting equation (21) on an elemental basis, and integrating over the element domain with Galerkin weighting results in the equation

$$\int_{D^e} \{N\} \left[\frac{\partial}{\partial x}\left(k_x \frac{\partial \tilde{T}^e}{\partial x}\right) + \frac{\partial}{\partial y}\left(k_y \frac{\partial \tilde{T}^e}{\partial y}\right)\right] t\, dD^e +$$
$$\int_{D^e} \{N\}\left[\alpha q_s - (h + h_e)(\tilde{T}^e - T_\infty)\right] dD^e = \{0\} \tag{25}$$

Green's theorem for a two dimensional integral is a means of integrating by parts and has the form

$$\int_D u(\nabla \cdot \vec{v})dD = \int_S u(\vec{v} \cdot \hat{n})dS - \int_D \vec{v} \cdot \nabla u\, dD \tag{26}$$

Applying this to the first integral in equation (25) with u taking the identity of N_i and $\nabla \cdot \vec{v}$ representing the differential operation on $\tilde{T}^e$ results in

$$\int_{D^e} \{N\}\left[\frac{\partial}{\partial x}\left(k_x \frac{\partial \tilde{T}^e}{\partial x}\right) + \frac{\partial}{\partial y}\left(k_y \frac{\partial \tilde{T}^e}{\partial y}\right)\right] t\, dx\, dy =$$
$$\int_{S^e} (\vec{q} \cdot \hat{n})\{N\}dS^e - \int_{D^e}\left[\left\{\frac{\partial N}{\partial x}\right\}k_x \frac{\partial \tilde{T}^e}{\partial x} + \left\{\frac{\partial N}{\partial y}\right\}k_y \frac{\partial \tilde{T}^e}{\partial y}\right] t\, dx\, dy \tag{27}$$

Substituting this result back into equation (25) and making the substitution for $\tilde{T}^e$ from equation (23), noting that

$$\frac{\partial \tilde{T}^e}{\partial \eta} = \lfloor \frac{\partial N}{\partial \eta} \rfloor \{T\}^e \tag{28}$$

gives the element equation

$$\int_{D^e}\left[k_x\left\{\frac{\partial N}{\partial x}\right\}\lfloor\frac{\partial N}{\partial x}\rfloor\{T\}^e + k_y\left\{\frac{\partial N}{\partial y}\right\}\lfloor\frac{\partial N}{\partial y}\rfloor\{T\}^e\right] t\, dx\, dy +$$
$$\int_{D^e}(h + h_e)\{N\}\lfloor N\rfloor\{T\}^e dx\, dy = \tag{29}$$
$$\int_{D^e}\left[\alpha q_s + (h + h_e)T_\infty\right]\{N\}dx\, dy - \int_{S^e}(\vec{q} \cdot \hat{n})\{N\}dS^e$$

where the boundary integral (S^e) represents element perimeter conditions. These terms are indicative of external heat loads that must be applied to maintain a boundary temperature. This equation may be written in a more concise manner as in equation (30)

$$\int_{D^e}[B]^T[k][B]\{T\}^e t\, dx\, dy + \int_{D^e}(h + h_e)\{N\}\lfloor N\rfloor\{T\}^e dx\, dy =$$
$$\int_{D^e}\left[\alpha q_s + (h + h_e)T_\infty\right]\{N\}dx\, dy - \int_{S^e}(\vec{q} \cdot \hat{n})\{N\}dS^e \tag{30}$$

where the matrices in the first integral are given by

$$[B] = \begin{bmatrix} \frac{\partial N_1}{\partial x} & \frac{\partial N_2}{\partial x} & \frac{\partial N_3}{\partial x} & \frac{\partial N_4}{\partial x} \\ \frac{\partial N_1}{\partial y} & \frac{\partial N_2}{\partial y} & \frac{\partial N_3}{\partial y} & \frac{\partial N_4}{\partial y} \end{bmatrix} \qquad [k] = \begin{bmatrix} k_x & 0 \\ 0 & k_y \end{bmatrix} \tag{31}$$

9

These integrations may be performed to assemble the element matrix equation

$$\left[[K_c] + [K_h] + [K_r]\right]\{T\}^e = \{R_q\} + \{R_h\} + \{R_r\} + \{R_T\} \tag{32}$$

where the individual matrices are composed as follows.

$$[K_c] = \int_{D^e} [B]^T[k][B]t\,dx\,dy$$

$$[K_h] = \int_{D^e} h\{N\}\lfloor N\rfloor dx\,dy$$

$$[K_r] = \int_{D^e} h_r\{N\}\lfloor N\rfloor dx\,dy$$

$$\{R_q\} = \int_{D^e} \alpha q_s\{N\}dx\,dy \tag{33}$$

$$\{R_h\} = \int_{D^e} hT_\infty\{N\}dx\,dy$$

$$\{R_r\} = \int_{D^e} h_r T_\infty\{N\}dx\,dy$$

$$\{R_T\} = -\int_{S^e} (\vec{q}\cdot\hat{n})\{N\}dS^e$$

The coefficient matrices $[K_c]$, $[K_h]$, and $[K_r]$ are element conductance matrices arising from conduction, convection, and radiation, respectively. The vectors $\{R_q\}$, $\{R_h\}$, $\{R_r\}$, and $\{R_T\}$ are heat load vectors resulting from incident radiant surface heating, surface convection, surface radiation from ambient surroundings, and specified nodal temperatures. It is noted that the radiant surface heating load vector and the surface radiation load vector may be combined to form a single load vector (reference 3), but are left seperate here for clarity since the radiant surface heating vector entries are obtained from a data file created by the radiant thermal load analysis. The resulting element matrices may then be assembled into the corresponding system matrices and solved linearly for the global temperature solution vector within a iterative loop for nonlinear contribution convergence.

GFE Fortran Code

The GFE finite element formulation was programmed to analyze the thermal response of thin panels to an arbitrary surface heat load. This code is fairly modular as is seen in the flow chart, appendix C. The analysis of the system shown in figure 3 may be performed for a horizontal or vertical configuration with one side radiantly heated. Either or both of the sides may be allowed to exchange heat with different (or the same) surroundings through forced convection, free convection, and radiation. Perimeter temperatures or heat loads may also be specified.

Upon execution, a preprocessor initializes system dependent parameters and control flags from a data file and uses this information throughout the execution process. This information includes system parameters (such as dimensions and configuration), control

10

flags (including constant property and surface condition flags), iteration parameters, and convergence criteria. Control is then passed to the main program where the element connectivity is established, the solution vector is initialized with initial guesses (and known temperatures), and the radiant surface heating load vector is initialized with data taken from a file created by the radiant heat load analysis. All subsequent calls to subroutines are made from this main program which include calls to subroutines providing thermal property data, evaluation of convective heat transfer coefficients, calculation of element matrix entries and assembly into the global system, and solution to the resulting set of system equations.

With dependence on previously set control flags, the program begins the direct iteration by setting the system properties (e.g. air and panel material themal properties) or interpolating the necessary data from cubically fitted thermal property data sets. All air and material properties may be allowed to vary with temperature. Using this data, the surface heating load is modified by specimen surface absorptivity (α), surface conditions (including the radiative nonlinearity) are established for each element, and the element contributions to the global system are assembled. The resulting linear set of equations are then solved by a Gaussian elimination technique for the new solution vector. The new solution vector is then altered for convergence enhancement due to the instability of the solution from the radiation nonlinearity. This altered vector is then checked for convergence based on its similarity to the altered solution in the previous iteration. The new vector is then returned for the next consecutive iteration upon unsuccessfull convergence, or passed for post-processing upon successfull convergence.

EAL Thermal Formulation

The thermal response analysis was also performed using the thermal analyzers of EAL. Based on information in the users manuals (references 4 and 5), it is apparent that the formulation used by the thermal analyzers is much more general but quite similar to that used in GFE with some exceptions. One such exception is the manner in which EAL accepts and uses the radiant thermal load.

EAL requires the radiant thermal load to be entered on an elementally averaged basis. This difference is due to the fact that the radiation elements included in the EAL formulation are assumed to have uniformly distributed incident heat flux [4]. GFE assumes the emissive power to be uniform over an element, but the incident heat flux is allowed to vary. This difference is of fairly slight consequence since, with a sufficiently fine finite element mesh, the pre-averaging would result in a less than significant deviation from the result produced by GFE. The only issue remaining here is the difference in computational effort required to obtain sufficiently similar resulting temperature distributions.

Another, more fundamental, formulation difference arises in the treatment of the radiation-exchange nonlinear surface condition. Recall that GFE evaluates this nonlinearity in advance by forming an effective radiation heat transfer coefficient. In this way, the nonlinear element conductance matrix entries are replaced by linear entries multiplied by a nonlinear parameter (known as the effective radiation heat transfer coefficient) which is evaluated with the other heat transfer coefficient(s) prior to element matrix assembly in

the iteration procedure. In contrast, an integral element equation similar to equation (29) would have the EAL form of

$$\int_{D^e} \left[k_x \left\{ \frac{\partial N}{\partial x} \right\} \left\lfloor \frac{\partial N}{\partial x} \right\rfloor \{T\}^e + k_y \left\{ \frac{\partial N}{\partial y} \right\} \left\lfloor \frac{\partial N}{\partial y} \right\rfloor \{T\}^e \right] t \, dx \, dy +$$

$$\int_{D^e} h_e \{N\} \lfloor N \rfloor \{T\}^e \, dx \, dy + \int_{D^e} \epsilon \sigma T^3 \{N\} \lfloor N \rfloor \{T\}^e \, dx \, dy = \qquad (34)$$

$$\int_{D^e} [\alpha q_r + h T_\infty] \{N\} \, dx \, dy - \int_{S^e} (\vec{q} \cdot \hat{n}) \{N\} \, dS^e$$

where the integral radiant emission term produces a diagonal radiation-conductance element matrix with entries given by

$$K_{ij} = \begin{cases} w_i T_i^3 & i = j \\ 0 & i \neq j \end{cases} \qquad (35)$$

The w_i are weighting factors which are determined by requiring that the total radiant energy emitted by the element be the same for both diagonal and non-diagonal matrices. This results in the *lumped formulation*

$$K_{ij} = \begin{cases} 4 T_i^3 \int_{D^e} \epsilon \sigma N_i \, dx \, dy & i = j \\ 0 & i \neq j \end{cases} \qquad (36)$$

where the terms represent the matrix entries of the diagonal radiation conductance matrix [3,4]. The radiant exchange load vector is handled by considering a summation of exchanges between all emitting and receiving surfaces. For the problem in consideration, this may be simplified to the load term q_r in equation (34) which represents the heat load (to complete the surface exchange) provided by the surroundings in addition to the incident heat due to the lamp emission. It is noted that in actually solving the given problem, the radiant surface heating load vector was increased by an amount $\alpha \sigma T_\infty^4$ and the specimen surface was allowed to radiate to absolute zero as is implied by equation (34).

THERMAL EXPERIMENTS

Radiant Heat Flux Measurements

The goal of these tests was to provide an accurate scaling factor (apparent lamp power) for the heat flux distribution analysis and to provide a means of comparing the normalized analytical results to measured radiant heat flux distributions. The experimental setup is shown in figure 5 which includes a single unreflected quartz radiant heater (rated at 1000 watts) suspended by a supporting fixture over a Gardon-type heat flux sensor. The support structure was painted highly absorptive black so that reflective irregularities in the radiant field could be minimized. A contribution to the radiant field from support structure elevated temperature emission was still expected but assumed more well behaved. The heat flux sensor was mounted with its receiving surface flush to the upper surface of a layer of Fiberfrax insulation. This mounting configuration was used in order to minimize anomalies

in the radiant field and/or measurement produced by a non-flat incident surface. The lamp power was supplied from a 440 V substation, stepped down to 240 V, and controlled by a variable transformer. In order to assure constant lamp operating conditions, the lamp input voltage was continuously monitored by a digital voltmeter. An overview of the entire experimental apparatus is shown in figure 6 where the particular test shown is a preliminary temperature measurement. The sensor output (in mV) was monitored by an additional voltmeter.

A cut-away view of the heat flux sensor is shown in figure 7. The sensor consists of a sensing foil, two thermocouple wires, and a water cooled copper heat sink. The sensor operation is based on the theory that the temperature gradient from the center of the sensing foil to the isothermal block is governed solely by the incident radiant flux. This is reasonable for this experiment since the sensor surface is highly absorptive ($\alpha = .89$) and the losses from the foil due to radiant emission and free convection are negligible. These losses are negligible since the surface area of the sensing foil is small (on the order of .08 cm^2) and the temperature difference between the foil and ambient surroundings is small relative to the corresponding temperature difference between the foil and lamp. Losses from the foil surface to the interior of the sensor are discounted by similar reasoning. Finally, the relatively short dimension of the foil surface allows the temperature profile to be assumed linear. Based on these conditions, the temperature difference measured by the attached thermocouple is directly proportional to the magnitude of the incoming radiant flux [6,7].

A series of tests were performed for varying lamp-to-sensor distances and varying lamp input power. Measurements were taken for lamp-to-sensor distances of 15.24 cm, 12.7 cm, and 7.62 cm. The tests conducted at 15.24 cm and 12.7 cm are restricted to full power (240 V) lamp operation. In contrast, the tests conducted at 7.62 cm include lamp input voltages of 240, 200, and 160 volts. Radiant heat flux measurements were recorded for each system arrangement and lamp input voltage at eleven positions along the axis of the lamp starting at one end of the filament and proceding to the other end in one inch increments. Similarly, four measurements in the transverse direction were recorded at positions in the incident plane of 2.54 cm and 5.08 cm in the negative y-direction and correspondingly in the positive y-direction. Since a portion of the support structure was in close proximity to and in direct contact with the lamp ends, it is certain that it attained an elevated temperature through conductive and radiative heating. The contribution to the radiant field from the lamp is known to reach a steady-state value almost instantaneously, however, the support structure contribution was expected to increase with time. Consequently, care was taken to assure that the radiant field was fully developed (supporting structure had time to reach temperature) and the lamp input power remained accurate and steady before recording each measurement. The radiant field was observed to be fully developed within a time lapse of 10 minutes for this particular system with the lamp operating at full power. A shorter time was required for the subsequent measurements in a sequence since the support structure remained at an elevated temperature for some time between measurements. This close attention was necessary in setting these and the geometric system parameters due to the sensitivity of radiant exchange to parameter changes.

Temperature Measurements

In an effort to validate the finite element thermal analyses, a series of temperature tests were performed. The test apparatus for the temperature measurements is shown in figure 8. These tests were conducted such that the system geometry and thermal conditions matched those of the corresponding heat flux experiments. The variable system parameters included lamp-to-specimen distance and time to steady-state. All of the temperature tests were performed with a lamp input voltage of 240 V.

The test apparatus consisted of the single unreflected quartz heater with the same suspension and energizing system as was used in the heat flux tests. The lamp input voltage was again continuously monitored by a digital voltmeter. The irradiated specimens included an AISI 347 stainless steel panel (10.16 cm x 17.92 cm x .127 cm) and a 6Al-4V titanium panel (10.16 cm x 22.23 cm x .127 cm). The stainless steel panel was instrumented with 13 type-J thermocouples as shown in figure 9. Likewise, the titanium panel was instrumented with 15 type-J thermocouples as shown in the same figure. The resulting temperatures in each test were monitored and recorded by a multichannel data logger. Measurements were taken as a function of time, but only the steady-state temperatures will be reported here since the analysis was limited to steady-state conditions.

As can be seen in figure 8, the upper surface of the panel was irradiated and allowed to exchange heat with the ambient surroundings. Since the lamp diameter is small relative to the other system dimensions, it was assumed that there were no reradiation exchanges between the panel and lamp. Also, with the same reasoning, it was assumed that the freely convecting flow was unimpeded by the lamp. The lower side of the panel was insulated by placing the specimen in a 2.54-cm bed of Q-Fiber Felt silica insulation which in turn rested upon a 2.54-cm layer of Zircar RS-100 fibrous ceramic insulation. The lower surface of the Zircar insulation was open to the ambient surroundings. The presence of this insulation strengthened the assumption of 'no temperature gradient' through the panel thickness.

The temperature gradient through the insulation was recorded using a thermocouple placed at the insulation interface and one placed on the underside of the Zircar insulation. This aided in establishing the lower surface boundary condition since a resistive analogy with temperature dependent insulation thermal properties was applied.

The insulation thermal conductivity temperature dependence was obtained from the respective manufacturer's data sheets [8,9]. Accordingly, the specimen material thermal conductivity temperature dependence was obtained from standard thermal property references [10,11]. Other important temperature dependent parameters, necessary for the analysis if this system, are the specimen radiative thermal surface properties.

The radiant surface properties of most materials are very sensitive functions of surface condition [12]. Therefore, measurement of these properties from the given specimen is the method of choice. However, exact measurements of this sort were not available during the period these tests were performed. Therefore, approximate measurements were made and were supplemented by values obtained from thermal radiative property references [12,13]. The radiative property measurements were inexact since the estimated total hemispherical

14

emittances were based on specular and diffuse reflectance measurements over a 2.5-16 micron spectral range. This spectral range accounts for about 60% of the blackbody distribution at 311 K, about 95% at 589 K, and about 25% at 2478 K. The thermal radiative property measurements are given in tables I and II in comparison to the values obtained from reference [12,13]. It is easily seen in this table that the data obtained from reference for the stainless steel panel is fairly accurate, much more so than that obtained for the titanium panel, noting that the temperature tests produced measurements ranging from 375 K to 490 K. It was decided that the data obtained from reference 12 for the stainless steel panel would be used for temperature prediction purposes since it is seen to be fairly accurate and the measured data did not allow for accurate extrapolation, especially at the lower temperatures. In contrast, the measured emissivity for the titanium panel corresponding to 589 K was used for prediction since the reference data was obviously somewhat missmatched and the measured data again did not allow for extrapolation. Therefore, the total hemispherical emittances incorporated into the analysis were .39 and .35 for the stainless steel and titanium panels respectively. It is noted that .39 is thought to be a more accurate representation of the stainless steel surface condition than .35 is of the titanium surface condition.

RESULTS AND COMPARISONS

Radiant Heat Flux

Incident radiant heat flux data were recorded for lamp-to-sensor distances of 7.62 cm, 12.7 cm, and 15.24 cm. The data recorded at the 12.7 cm and 15.24 cm distances is limited to full power (240 V) lamp operation, but the data recorded at three 7.62 cm includes measurements at lamp input voltages of 240, 200, and 160 volts. The resulting measured distributions of radiant heat flux in the longitudinal and transverse directions are shown in figures 10 through 19 in comparison with analytically predicted curves. The tick mark labeling results from considering the origin of the incident surface spatial axes to be directly below the center of the lighted length (figure 1). This data is also tabulated as seen in tables III and IV.

The longitudinal measurements correspond to traversing the sensor from the left end of the 25.4 cm lighted filament to the right in 2.54 cm increments, as seen in figure 5. The transverse measurements correspond to traversing the sensor from a location 5.08 cm in front of the lamp to a location 5.08 cm behind the lamp along a line below, perpendicular to, and passing through the center of the lamp axis.

It should be recognized that the flux prediction technique is limited to distribution predictions and is therefore scaled by an apparent power extracted from equation (16) using the central most measurement in each comparison. The central point was chosen for a scaling measurement since the geometry for this position is most accurate (and reproducible) and the support structure contribution to the radiant field is relatively low.

The possibility of support structure radiation involvement can be seen in the comparison figures. Note that in all longitudinal comparisons the measurements at locations nearer the ends of the lighted length have an increasing trend relative to the prediction curve.

15

This trend is seen to increase with decreasing lamp-to-sensor distance (figures 10, 12, and 14). In these figures the maximum relative differences are 1.4%, 4.4%, and 5.4% respectively. The transverse results show an increasing experimental asymmetry with respect to the lamp axis with decreasing lamp-to-sensor distance (figures 11, 13, and 15). These results can be explained by the fact that the radiant interaction of the support structure has an increasing effect as the sensor is moved closer to the structure in the incident plane. It is also noted that at a distance of 15.24 cm the radiant asymmetry is indetectable (figure 11), marking the spatial limit of the imperfect boundary condition significance.

The apparent power (Q_0) discussed above is both a function of geometry and lamp input power due to changes in the radiant efficiency resulting from changes in loss contributing factors. The variation of the apparent power with lamp input voltage is shown in figure 20 for a lamp to sensor distance of 7.62 cm. A corresponding plot of apparent power as a function of lamp-to-sensor distance at a lamp input voltage of 240 V is shown in figure 21. The apparent power is seen to have a linear variation with respect to either independent variable with a maximum deviation from least squares fit of 1.18% in figure 20 and 0.92% in figure 21.

Specimen Temperature

Temperature measurements using the two thin metallic panels were conducted with geometric conditions equivalent to those used in the flux tests. The observations that were made about the accuracy of the thermal radiative properties of the individual panels were reinforced by the results obtained in preliminary tests. Therefore, a majority of the results presented here are from tests performed with the stainless steel panel.

Surface temperatures on the stainless steel panel were recorded for lamp-to-panel distances of 7.62 cm, 12.7 cm, and 15.24 cm while those on the titanium panel were recorded at the 7.62 cm and 15.24 cm distances only. The longitudinal and transverse distributions correspond to measurements made with type-J thermocouples mounted to the underside of each panel (figure 9), while the specimens were oriented with respect to the lamp as shown in figure 8. The results associated with the tests conducted on the stainless steel panel are shown in figures 22 through 35 (tables V, VI, and VII); results for the titanium panel are shown in figures 36 through 39 (tables VIII and IX). The tick mark labeling in these plots is consistent with the labeling used in the plots of radiant heat flux (figure 3).

The following discussion will concentrate on the tests conducted at the lamp-to-panel distance of 7.62 cm since this distance was the most extensively tested. From figure 22, it can be seen that both GFE and EAL predict the longitudinal temperature distribution very well. However, there are some differences between analysis and experiment and between the two analyses which seem to be accountable.

Referring again to figure 22, the difference in temperature gradient between prediction curves probably results from the use of the element averaged radiant heat load in EAL. This tends to reduce the maximum flux (occurring at the center) and increase the minimum flux (occurring at both ends). Coupling this effect with the fact that EAL retains the specimen radiant emission nodal dependancy in its formulation of the radiation boundary condition

(EAL Thermal Formulation), which tends to counteract the effects of the averaged heat load, alludes to some of the resulting differences. The analysis of the free convection surface condition is a factor producing the somewhat uniform offset between prediction curves. In analyzing the convective data for each run, it was found that the free convection coefficient calculated by EAL was an average of approximately 1% higher than that calculated by GFE. This discrepancy is a result of roundoff error associated with incorporating relatively few digits in the EAL free convection correlation parameter data table. It is also noted that both analyses assumed an insulated perimeter which is apparent in the results by the persistent difference between analysis and experiment at the edges (analysis is high as expected). This result should only be slightly affected by the radiant field 'fringing' since the measured deviation from the predicted heat flux distribution is most significant outside of the specimen dimensions (figures 10, 12, 14, 16, 18).

The transverse temperature distribution (figure 23) shows an experimental asymmetry which is accountable through two observations. The support structure contribution to the radiant field has a temperature increasing effect on the portion of the panel toward the support structure from the lamp centerline. In the direction away from the support structure beyond the lamp centerline, a reduction in insulation uniformity, due to the presence of themocouple wires, has a temperature decreasing effect beyond the already imperfectly insulated perimeter. This reasoning is supported by figures 24 and 25 which show corresponding results after the panel was rotated 180 degrees about its vertical axis. In this configuration, the thermocouple wire exit and the radiation 'hot spot' coincide and tend to cancel as seen in figure 25.

Other variations on this test that should be mentioned include a experimental reproducibility test and a check on EAL's convection analysis. The reproducibility of the temperature test procedure was quantified by completely disassembling the test apparatus and specimen/insulation assembly followed by the reconstruction of the experimental conditions which produced the results shown in figures 22 and 23. The reproducibility of the tests proved to be good as seen in figures 26 and 27. The effort involved in reproducing the experiment geometry and boundary conditions was no more tedious than the initial test, however, these experiments were in general very difficult to perform with sufficient accuracy, as will be seen in the discussion of other results. A note with respect to EAL's convective analysis is demonstrated in figures 28 and 29. The grossly inaccurate curve is one predicted by EAL when allowed to choose the convective 'correlation parameters' automatically, based on convective system parameters. The other curve generated by EAL is one for which the convective correlation parameters were forced to coincide with those used by GFE. Two standard sets of correlation parameters corresponding to laminar or turbulent conditions result from basic boundary layer theory [1,14]. GFE selects the applicable correlation parameters based on the flow field Rayleigh number. Once GFE selected the necessary correlation parameters for a particular analysis, these values were then used as input data in the EAL free convection parameter data set. This procedure was used in all of the EAL predictions presented here, resulting in the above mentioned 1% difference in free convection coefficients. This discussion is not intended to discount the validity of EAL's convective analysis, but to emphasize the caution necessary to attain satisfactory results when applying such analyses to specific problems.

Figures 30 through 35 represent the comparisons established for the stainless steel panel at the 12.7 cm and 15.24 cm lamp-to-panel distances. The results presented in these plots typically show more erratic and uniform differences between analysis and experiment than the previous results. This is probably a result of increased experimental error. Since the experiments at these lamp-to-panel distances were actually conducted prior to the previously discussed results, they were more apt to have significant experimental error. Two definite factors influencing these earlier results are Q-Fiber felt insulation nonuniformities and time to steady-state estimation.

Figure 30 is an example of a test where the time to steady-state was probably underestimated. Note that the entire measured distribution is below the theoretical curves. This problem propagated through most of the earlier tests on the stainless steel panel where in some cases the time was possibly overestimated. It was then established that steady-state conditions were met when the temperature measurement of the greatest magnitude first showed oscillation within fractions of a degree Celsius. The accuracy of the previously discussed results (lamp-to-panel distance of 7.62 cm) is partially a result of this observation. Figures 31 and 32 illustrate the problem of ensuring uniform surface insulation on the underside of the panel. The relatively large asymmetry in figure 31 is due to the same thermocouple wire exit problem that existed in the subsequent results but to a greater degree. The asymmetry seen in figure 32 is a result of reinsulating the panel to improve the transverse distribution while inadvertently producing a nonuniformity in the longitudinal direction.

The results shown in figure 36 (titanium panel) show an offset that is thought to be due the the fact that an upper limit of the surface emissivity (.35) was used for the temperature prediction. Through analytical experimentation with varying the emissivity, and thus the surface absorptivity (greybody), it was found that a lower emissivity value would lower the magnitude of the temperature distribution. This observation emphasizes the fact that the incident radiant heat flux is the most significant driving factor in this thermal problem. Another problem, which is more apparent in figure 38, is the apparent local decrease in temperature at the central thermocouple locations. This effect was a result of the lack of sufficient insulation in that vacinity. The insulation nonuniformity occured in this location since all of the thermocouple wires were collected there and routed toward one side of the panel. This phenomenon can be seen in all of the results (figures 22, 24,..., 36, 38) although it is most apparent in figures 36 and 38 due to the close thermocouple placement near the center of the titanium panel, figure 9.

CONCLUDING REMARKS

A method of predicting the distribution of radiant heat flux produced on a flat incident surface by a bank of quartz heaters has been tested and experimentally verified. This method is limited to planar arrays of quartz heaters with a single flat reflector. The theory was applied to a radiant system consisting of a single unreflected lamp irradiating a flat surface parallel to the lamp axis. Due to the nonconservative energy conversion and transfer in the quartz heater, it was determined that the radiative power of the lamp had to be quantified by a single experimental measurement. This measurement was then incor-

porated into the analysis to extract a normalization factor for the predicted radiant heat flux distribution. Variations in this normalization factor (parameter dependent apparent power) with lamp input voltage and lamp-to-sensor distance were found to be linear for the parameter ranges presented here. The theory was experimentally verified and shown to produce accurate predictions of the incident radiant heat flux distribution for variable lamp-to-sensor distance and variable lamp input power.

Two finite element thermal analyses were applied to the two dimensional heat transfer in thin metallic plates with conductive, convective, and radiative surface conditions forced by a radiant surface heat load. A steady-state, two-dimensional thermal analysis formulation based on Galerkin's Method of Weighted Residuals (GFE) was formulated specifically for this problem and the thermal analyzers of the Engineering Analysis Language (EAL) were also applied. The finite element analyses were analytically consistent and performed well in prediction of surface temperature distributions on thin metallic panels exposed to radiant heat. Some differences between the analyses were found, however, in the formulation of boundary conditions. It was found that EAL's formulation of the specimen radiant emission may provide somewhat better prediction of the radiant loss distribution, however, the elementally averaging treatment of incident surface heating may induce a loss of resulting temperature distribution accuracy. The 'automatic' convective analysis incorporated by EAL proved to provide inaccurate results in application to this problem. Upon forcing the appropriate convective correlation parameters, however, EAL produced significantly better results as expected. The differences between results produced by analysis and by experiment (and between analyses) were discussed with reference to explicit experimental and analytical error contributing factors.
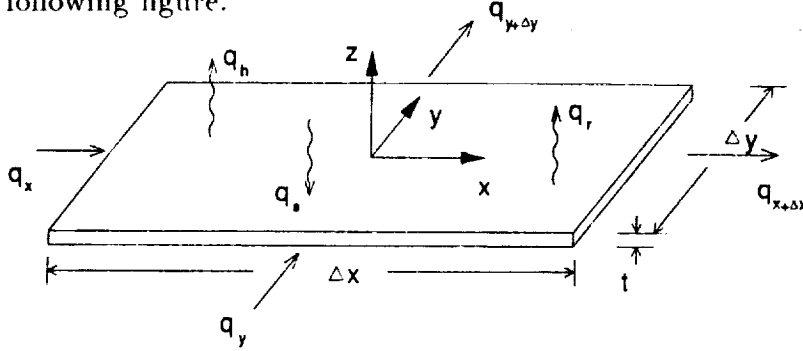
ACKNOWLEDGEMENTS

APPENDIX A

HEAT BALANCE IN A THIN PLATE

The geometry associated with the heat balance in a differential portion of a thin plate is shown in the following figure.

The steady-state heat balance in this element is represented by

$$\left(net\ heat\ conducted\ in\right) + \left(net\ heat\ exchanged\ with\ surroundings\right) = 0 \qquad (A.1)$$

which may be written in terms of the differential heat loads as

$$dQ_x - dQ_{x+\triangle x} + dQ_y - dQ_{y+\triangle y} + dQ_s - dQ_r - dQ_h = 0 \qquad (A.2)$$

where the first two terms represent the net heat conducted in the x-direction, the second two represent the net heat conducted in the y-direction, dQ_s is the differential incident radiant energy, and dQ_r and dQ_h are the differential surface heat losses due to radiant and convective exchange respectively. If a first-order Taylor Series representation of $dQ_{\eta+\triangle\eta}$, given by

$$dQ_{\eta+\triangle\eta} = dQ_\eta + \frac{\partial Q_\eta}{\partial \eta}\triangle\eta \qquad (A.3)$$

is substituted into equation A.2, then the equation may be written in the form

$$dQ_x - \left(dQ_x + \frac{\partial Q_x}{\partial x}\triangle x\right) + dQ_y - \left(dQ_y + \frac{\partial Q_y}{\partial y}\triangle y\right) + dQ_s - dQ_r - dQ_h = 0 \quad (A.4)$$

The heat loads appearing in equation (A.4) may be written in more recognizeable terms by applying the appropriate heat transfer relations.

$$dQ_x = -k_x \frac{\partial T}{\partial x} t\triangle y$$

$$dQ_y = -k_y \frac{\partial T}{\partial y} t\triangle x$$

$$dQ_s - dQ_r = \alpha dq_s \triangle x\triangle y - \epsilon\sigma\left(T^4 - T_\infty^4\right)\triangle x\triangle y \qquad (A.5)$$

$$dQ_h = h\left(T - T_\infty\right)\triangle x\triangle y$$

20

where k_x and k_y are the material thermal conductivities, t is the plate thickness, T is the surface temperature, T_∞ is the surroundings temperature, ϵ is the specimen surface emissivity, α is the specimen surface absorptivity, and σ is Stefan-Boltzmann's constant. The convective heat transfer coefficient (h) may be composed of free and/or forced convection contributions from one or both sides of the plate. The radiant exchange term may be multiplied by a factor of value 1 or 2 depending on whether the radiant exchange is to be considered from one or both sides of the plate. Incorporating these relations into equation (A.4), the heat balance may be written in the form

$$\frac{\partial}{\partial x}\left(k_x \frac{\partial T}{\partial x}\right)t\triangle x\triangle y + \frac{\partial}{\partial y}\left(k_y \frac{\partial T}{\partial y}\right)t\triangle x\triangle y +$$
$$\left[\alpha dq_s - h(T - T_\infty) - \epsilon\sigma\left(T^4 - T_\infty^4\right)\right]\triangle x\triangle y = 0 \qquad (A.6)$$

Canceling the differential area from this equation leaves the heat balance per unit area

$$\left[\frac{\partial}{\partial x}\left(k_x \frac{\partial T}{\partial x}\right) + \frac{\partial}{\partial y}\left(k_y \frac{\partial T}{\partial y}\right)\right]t = h(T - T_\infty) + \epsilon\sigma(T^4 - T_\infty^4) - \alpha dq_s \qquad (A.7)$$

This equation governs the temperature field on the surface of a differential portion of a thin orthotropic panel as affected by incident surface radiation and convective and radiative exchange boundary conditions. Since the equation is written on the per unit area basis, it may be immediately expanded to the finite area plate where the incident surface heating per unit area is given by q_s.

$$\left[\frac{\partial}{\partial x}\left(k_x \frac{\partial T}{\partial x}\right) + \frac{\partial}{\partial y}\left(k_y \frac{\partial T}{\partial y}\right)\right]t = h(T - T_\infty) + \epsilon\sigma(T^4 - T_\infty^4) - \alpha q_s \qquad (A.8)$$

APPENDIX B

GALERKIN'S METHOD OF WEIGHTED RESIDUALS

The method of weighted residuals as applied to an arbitrary differential equation

$$F(\phi) - f = 0 \qquad\qquad (B.1)$$

is explained as follows. The continuous field variable ϕ may be replaced by an approximate solution based on an assumed functional behavior of ϕ. This approximation may be written as

$$\phi \approx \tilde{\phi} = \sum_{i=1}^{m} N_i C_i \qquad\qquad (B.2)$$

where the N_i are the assumed functions of the independent variables and the C_i are the unknown dependent parameters [4]. If this approximation is substituted into the governing equation it is probable that the equation will not be satisfied exactly, leaving a residual. i.e.

$$F(\tilde{\phi}) - f = R \qquad\qquad (B.3)$$

The method of weighted residuals attempts to solve this equation for the unknowns (C_i) by forming a weighted average of the residual such that the average vanishes over the entire solution domain. Applying this to equation $(B.3)$ results in

$$\int_D \left[F(\tilde{\phi}) - f \right] W_i dD = \int_D R W_i dD = 0 \qquad\qquad i = 1, m \quad (B.4)$$

Choosing weighting functions such that they are equivalent to the assumed functions representing ϕ is known as Galerkin's method which gives

$$\int_D \left[F(\tilde{\phi}) - f \right] N_i dD = 0 \qquad\qquad i = 1, m \quad (B.5)$$

This equation, upon integration, results in a set of m equations which may be solved for the unknown dependent parameters C_i.
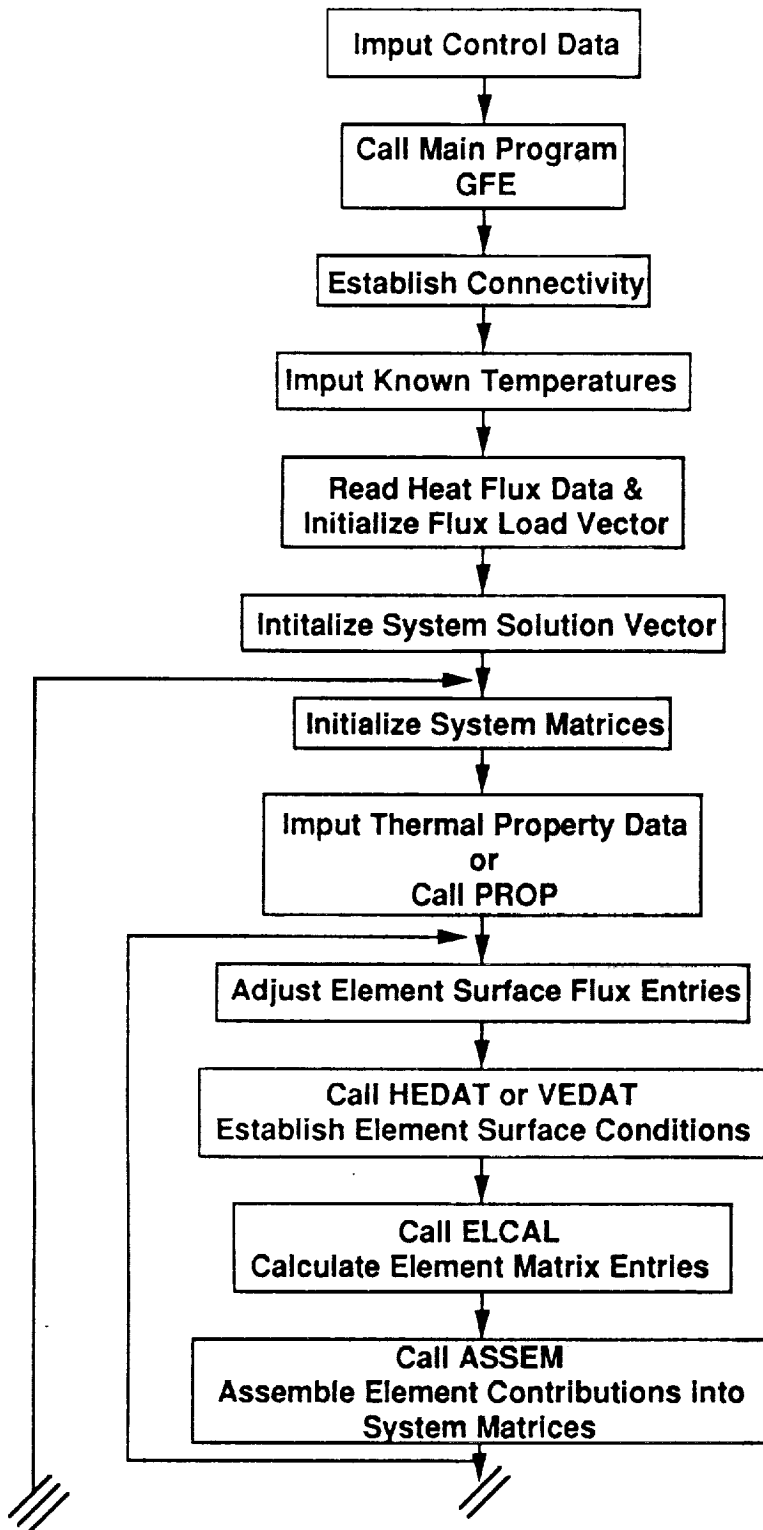
Since this method is applicable to the entire solution domain, it is equally applicable to any subdivision or element of the solution domain. In this way, the assumed functions (N_i) take on the identity of interpolation functions and are defined over an element. A similar discussion of the remaining terms in equation $(B.5)$ results in
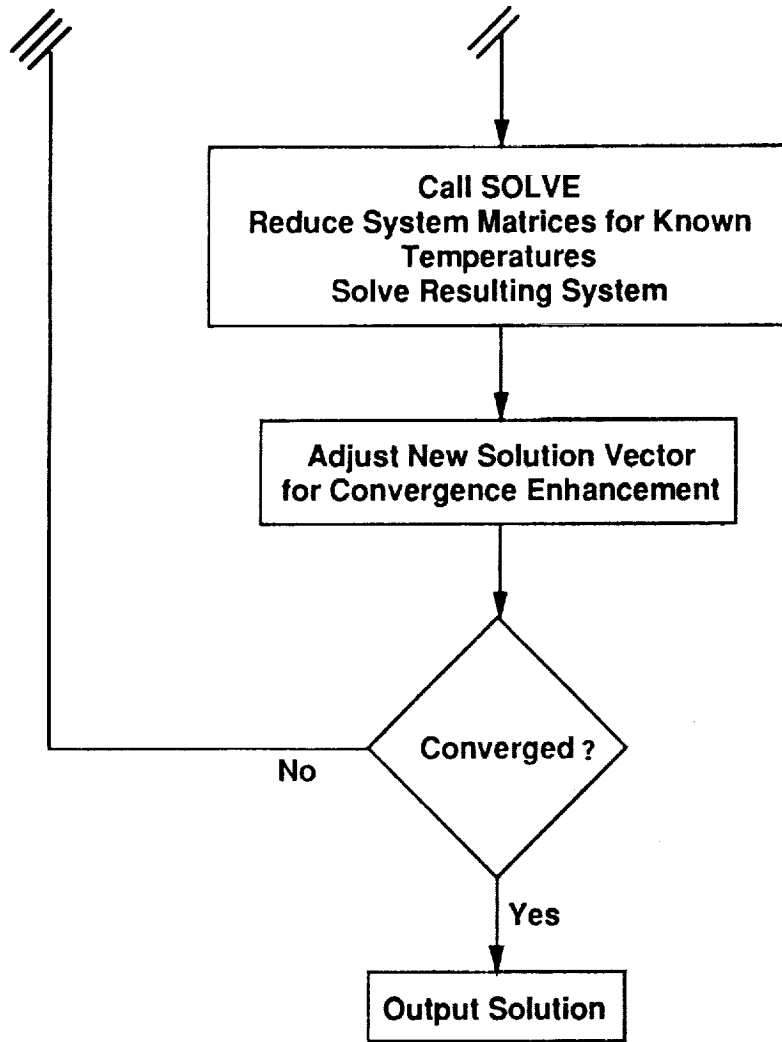
$$\int_{D^e} \left[F(\tilde{\phi})^e - f^e \right] N_i^e dD^e = 0 \qquad\qquad i = 1, r \quad (B.6)$$

where r is the number of nodes in an element.

22

GFE PROGRAM FLOWCHART

```
┌──────────────────────────┐
│     Imput Control Data    │
└──────────────────────────┘
              │
              ▼
┌──────────────────────────┐
│     Call Main Program     │
│            GFE            │
└──────────────────────────┘
              │
              ▼
┌──────────────────────────┐
│   Establish Connectivity  │
└──────────────────────────┘
              │
              ▼
┌──────────────────────────┐
│  Imput Known Temperatures │
└──────────────────────────┘
              │
              ▼
┌──────────────────────────┐
│    Read Heat Flux Data &  │
│  Initialize Flux Load Vector │
└──────────────────────────┘
              │
              ▼
┌──────────────────────────┐
│ Intitalize System Solution Vector │
└──────────────────────────┘
              │
              ▼
┌──────────────────────────┐
│  Initialize System Matrices │
└──────────────────────────┘
              │
              ▼
┌──────────────────────────┐
│  Imput Thermal Property Data │
│             or            │
│         Call PROP         │
└──────────────────────────┘
              │
              ▼
┌──────────────────────────┐
│ Adjust Element Surface Flux Entries │
└──────────────────────────┘
              │
              ▼
┌──────────────────────────┐
│     Call HEDAT or VEDAT   │
│ Establish Element Surface Conditions │
└──────────────────────────┘
              │
              ▼
┌──────────────────────────┐
│        Call ELCAL         │
│ Calculate Element Matrix Entries │
└──────────────────────────┘
              │
              ▼
┌──────────────────────────┐
│        Call ASSEM         │
│ Assemble Element Contributions into │
│       System Matrices     │
└──────────────────────────┘
```

```
              ///                        //
                                          |
                                          ▼
                    ┌─────────────────────────────────────────┐
                    │              Call SOLVE                  │
                    │   Reduce System Matrices for Known       │
                    │              Temperatures                │
                    │         Solve Resulting System           │
                    └─────────────────────────────────────────┘
                                          |
                                          ▼
                    ┌─────────────────────────────────────────┐
                    │         Adjust New Solution Vector       │
                    │        for Convergence Enhancement       │
                    └─────────────────────────────────────────┘
                                          |
                                          ▼
                                       ╱╲
                                     ╱    ╲
                                   ╱        ╲
          No                    ╱  Converged ? ╲
                                ╲              ╱
                                   ╲        ╱
                                     ╲    ╱
                                       ╲╱
                                        |
                                       Yes
                                        |
                                        ▼
                            ┌───────────────────────┐
                            │    Output Solution     │
                            └───────────────────────┘
```

24

REFERENCES

1. White, F. M.: Heat Transfer. Addison-Wesley Publishing Company, Inc. 1984. pp. 378-390.

2. Özişik, M. N.: Radiative Transfer and Interactions with Conduction and Convection. John Wiley and Sons, Inc. 1980. pp.15-16.

3. Huebner, K. H.; and Thornton, E. A.: The Finite Element Method for Engineers. John Wiley and Sons, Inc. 1982. pp. 108-112.

4. EISI-EAL User's Manual: Engineering Analysis Language Thermal Analysis Processors. V-2 Theory. Engineering Information Systems, May 1984. pp. TA2 4-1, TA2 2-5 and 2-6.

5. EISI-EAL User's Manual: Engineering Analysis Language Thermal Analysis Processors. V-1 Program Execution. Engineering Information Systems, May 1984.

6. Rall, D. L.; and Stempel, F. C.: A Discussion of the Standardized Procedure for Calibrating Heat Flux Transducers. Hy-Cal Engineering. 19th Annual ISA Conference and Exhibit. October 12-15, 1964. New York.

7. Malone, E. W.: Design and Calibration of Thin Foil Heat Flux Sensors. Instrument Society of America. 22nd Annual ISA Conference and Exhibit. September 11-14, 1967. Chicago, Illinois. P6-2-PHYMMID-67.

8. Manville Products Corporation. Q-Fiber Felt Insulation Data Bulletin. 1989.

9. Zircar Products, Inc. Technical Data Bulletin No. ZPI-700. June 1, 1987.

10. Peckman, D.; and Berstein, I. M.: Handbook of Stainless Steels. McGraw-Hill Inc. 1977.

11. Thermal Properties of Nonferous Metals and Alloys. Handbook of Military Standards V2. MIL-HDBK-5B. 1 September 1971. pp. 5-74.

12. Touloukian, Y. S.: Thermophysical Properties of High Temperature Solid Materials. Thermophysical Property Research Center, Purdue University. 1967.

13. Sala, A.: Radiant Properties of Materials. Polish Scientific Publishers. Warszawa. 1986.

14. Karlekar, B. V.; and Desmond, R. M.: Heat Transfer. West Publishing Company. 1982.

TABLE I.- AISI 347 STAINLESS STEEL TEMPERATURE DEPENDENT MATERIAL PROPERTIES

AISI 347 Stainless Steel Panel			
Temperature	Thermal Conductivity	Surface Emissivity	
K	W/m · K	Measurement	Reference [13]
300	16.61		.39
311	-	.26 @ 60%	.39
350	17.13		.39
400	17.65		.39
450	18.14		.39
500	18.69		.39
550	19.18		.39
589	-	.41 @ 95%	.39
600	19.64		.39
650	20.16		.39
700	20.66		.39
750	21.37		.395
800	22.15		.398
850	22.88		.40
900	23.68		.41
950	24.40		.42
1000	25.23		.437
1100	26.76		.505
2478	-	.55 @ 25%	-

TABLE II.- 6AL-4V TITANIUM TEMPERATURE DEPENDENT MATERIAL PROPERTIES

6Al-4V Titanium Panel			
Temperature	Thermal Conductivity	Surface Emissivity	
K	W/m · K	Measurement	Reference [14]
300	7.27		.287
311	-	.18 @ 60%	-
350	7.39		.357
400	7.70		.380
450	8.22		.400
500	8.83		.425
550	9.40		.450
589	-	.35 @ 95%	-
600	10.02		.475
650	10.59		.505
700	11.16		.535
750	11.77		.570
800	12.37		.610
850	12.98		.640
900	13.53		.655
950	14.19		.655
1000	14.75		.630
1100	15.92		-
2478	-	.60 @ 25%	-

Note: Measurement percentages indicate blackbody spectral portions.

TABLE III.- RADIANT HEAT FLUX COMPARISON DATA FOR LAMP-TO-SENSOR DISTANCES OF 15.24 cm AND 12.7 cm

Radiant Heat Flux, W/m^2				
Nodal	Figures 10 and 11		Figures 12 and 13	
Location	Measurement	Prediction	Measurement	Prediction
-12.70	2225.75	2202.44	2888.74	2748.55
-10.16	2699.31	2651.58	3409.66	3424.73
-7.62	3030.83	3036.83	3977.96	3988.32
-5.08	3314.96	3322.53	4404.17	4386.15
-2.54	3457.04	3494.66	4546.22	4614.64
0.0	3551.74	3551.75	4688.31	4688.30
2.54	3457.04	3494.66	4593.57	4614.64
5.08	3314.96	3322.53	4356.79	4386.15
7.62	3078.18	3036.83	3977.96	3988.32
10.16	2651.96	2651.58	3409.66	3424.73
12.70	2225.75	2202.44	2936.09	2748.55
-5.08	3078.18	3112.86	3788.52	3920.76
-2.54	3409.66	3432.49	4404.17	4473.25
0.0	3551.74	3551.75	4688.31	4688.30
2.54	3409.66	3432.49	4451.52	4473.25
5.08	3078.18	3112.86	3930.61	3920.76

TABLE IV.- RADIANT HEAT FLUX COMPARISON DATA FOR A LAMP-TO-SENSOR DISTANCE OF 7.62 cm AND LAMP INPUT VOLTAGES OF 240, 200, AND 160 VOLTS

Radiant Heat Flux, W/m^2				
Nodal	Figures 14 and 15		Figures 16 and 17	
Location	Measurement	Prediction	Measurement	Prediction
-12.70	4972.44	4677.63	3646.44	3476.97
-10.16	6677.27	6531.84	4877.74	4855.23
-7.62	7813.83	7794.20	5824.87	5793.58
-5.08	8429.48	8465.32	6251.05	6292.43
-2.54	8713.61	8769.44	6487.84	6518.49
0.0	8855.66	8855.68	6582.57	6582.59
2.54	8713.61	8769.44	6440.49	6518.49
5.08	8429.48	8465.32	6251.05	6292.43
7.62	7813.83	7794.20	5777.49	5793.58
10.16	6677.27	6531.84	4830.36	4855.23
12.70	4925.09	4677.63	3599.09	3476.97
-5.08	5682.79	5917.98	4262.09	4398.94
-2.54	7766.48	7900.00	5777.49	5872.22
0.0	8855.66	8855.68	6582.57	6582.59
2.54	8097.97	7900.00	6016.65	5872.22
5.08	6061.65	5917.98	4546.22	4398.94

Nodal	Figures 18 and 19	
Location	Measurement	Prediction
-12.70	2557.26	2401.36
-10.16	3409.66	3353.26
-7.62	4025.31	4001.32
-5.08	4356.79	4345.85
-2.54	4546.22	4501.98
0.0	4546.22	4546.26
2.54	4546.22	4501.98
5.08	4356.79	4345.85
7.62	4025.31	4001.32
10.16	3409.66	3353.26
12.70	2557.26	2401.36
-5.08	2936.09	3038.12
-2.54	4025.31	4055.64
0.0	4546.22	4546.26
2.54	4167.39	4055.64
5.08	3125.53	3038.12

TABLE V.- TEMPERATURE COMPARISON DATA FOR THE STAINLESS STEEL PANEL
WITH A LAMP-TO-SPECIMEN DISTANCE OF 7.62 cm

Tabulated Data for Figures 22 through 29			
Nodal	Temperature, K		
Location	Measurement 1	GFE Prediction	EAL (Unforced)
-10.16	470.39	471.75	521.16
-7.62	474.96	476.16	524.86
-5.08	482.70	482.33	530.83
-2.54	488.45	486.56	535.06
0.0	487.87	487.99	536.52
2.54	487.44	486.56	535.06
5.08	482.93	482.33	530.83
7.62	475.67	476.16	524.86
10.16	469.41	471.75	521.16
-5.08	475.85	478.66	527.70
-2.54	482.67	483.82	532.51
0.0	488.45	487.99	536.52
2.54	485.99	483.22	532.51
5.08	482.05	478.66	527.70
Location	Measurement 2	EAL (Forced)	Measurement Repro.
-10.16	468.19	471.43	471.62
-7.62	474.33	475.13	475.01
-5.08	482.14	481.05	481.64
-2.54	487.12	485.21	487.43
0.0	488.46	486.63	488.43
2.54	488.82	485.21	487.39
5.08	484.27	481.05	482.35
7.62	476.75	475.13	475.62
10.16	471.22	471.13	469.19
-5.08	478.11	477.68	474.63
-2.54	483.69	482.57	481.12
0.0	488.46	486.63	488.43
2.54	485.02	482.57	487.01
5.08	479.92	477.68	481.84

TABLE VI.- TEMPERATURE COMPARISON DATA FOR THE STAINLESS STEEL
PANEL WITH A LAMP-TO-SPECIMEN DISTANCE OF 12.7 cm

Tabulated Data for Figures 30 through 33				
Nodal	Temperature, K			
Location	Measurement 1	Measurement 2	GFE Prediction	EAL Prediction
-10.16	406.40	407.88	408.37	408.46
-7.62	409.18	410.31	410.88	410.66
-5.08	413.79	414.40	414.98	414.60
-2.54	417.02	417.70	418.13	417.69
0.0	417.31	418.93	419.27	418.82
2.54	416.77	419.32	418.13	417.69
5.08	413.73	416.76	414.98	414.60
7.62	409.37	412.81	410.88	410.66
10.16	405.19	410.28	408.37	406.46
-5.08	413.23	416.94	416.76	416.40
-2.54	415.26	417.86	418.18	417.75
0.0	417.31	418.93	419.27	418.82
2.54	417.67	418.92	418.18	417.75
5.08	416.17	417.22	416.76	416.40

TABLE VII.- TEMPERATURE COMPARISON DATA FOR THE STAINLESS STEEL
PANEL WITH A LAMP-TO-SPECIMEN DISTANCE OF 15.24 cm

Tabulated Data for Figures 34 and 35			
Nodal	Temperature, K		
Location	Measurement	GFE Prediction	EAL Prediction
-10.16	386.25	386.59	386.90
-7.62	389.41	388.43	388.51
-5.08	393.51	391.53	391.49
-2.54	395.93	393.97	393.87
0.0	395.52	394.87	394.75
2.54	394.96	393.97	393.87
5.08	392.23	391.53	391.49
7.62	388.18	388.43	388.51
10.16	384.37	386.59	386.90
-5.08	392.46	393.39	393.35
-2.54	394.36	394.23	394.14
0.0	395.52	394.87	394.75
2.54	396.33	394.23	394.14
5.08	395.39	393.39	393.35

TABLE VIII.- TEMPERATURE COMPARISON DATA FOR THE TITANIUM PANEL WITH A LAMP-TO-SPECIMEN DISTANCE OF 7.62 cm

Tabulated Data for Figures 36 and 37			
Nodal	Temperature, K		
Location	Measurement	GFE Prediction	EAL Prediction
-11.11	447.67	453.72	453.61
-8.57	456.37	462.01	460.73
-6.03	466.90	472.91	471.29
-3.49	473.69	480.17	478.49
-0.95	476.38	483.37	481.69
0.0	476.07	483.62	481.94
0.95	476.46	483.37	481.69
3.49	474.85	480.17	478.49
6.03	468.46	472.91	471.29
8.57	458.06	462.01	460.73
11.11	451.06	453.72	453.61
-5.08	460.93	468.14	467.15
-2.54	469.37	476.83	475.34
0.0	476.07	483.62	481.94
2.54	474.02	476.83	475.34
5.08	466.34	468.14	467.15

TABLE IX.- TEMPERATURE COMPARISON DATA FOR THE TITANIUM PANEL WITH A LAMP-TO-SPECIMEN DISTANCE OF 15.24 cm

Tabulated Data for Figures 38 and 39			
Nodal	Temperature, K		
Location	Measurement	GFE Prediction	EAL Prediction
-11.11	375.69	375.97	376.42
-8.57	379.45	379.18	379.29
-6.03	384.18	384.40	384.37
-3.49	387.74	388.65	388.56
-0.95	389.51	390.79	390.68
0.0	389.57	390.97	390.85
0.95	389.77	390.79	390.68
3.49	388.70	388.65	388.56
6.03	385.77	384.40	384.37
8.57	380.97	379.18	379.29
11.11	377.52	375.97	376.42
-5.08	386.28	388.35	388.36
-2.54	388.38	389.86	389.76
0.0	389.57	390.97	390.85
2.54	389.08	389.86	389.76
5.08	386.20	388.35	388.36

L

dA_l dA_c

Z $\hat{n}_l$ dQ_s

Θ_l r

Θ_s dA_s

ϕ_r

X'   H

ϕ Y

X
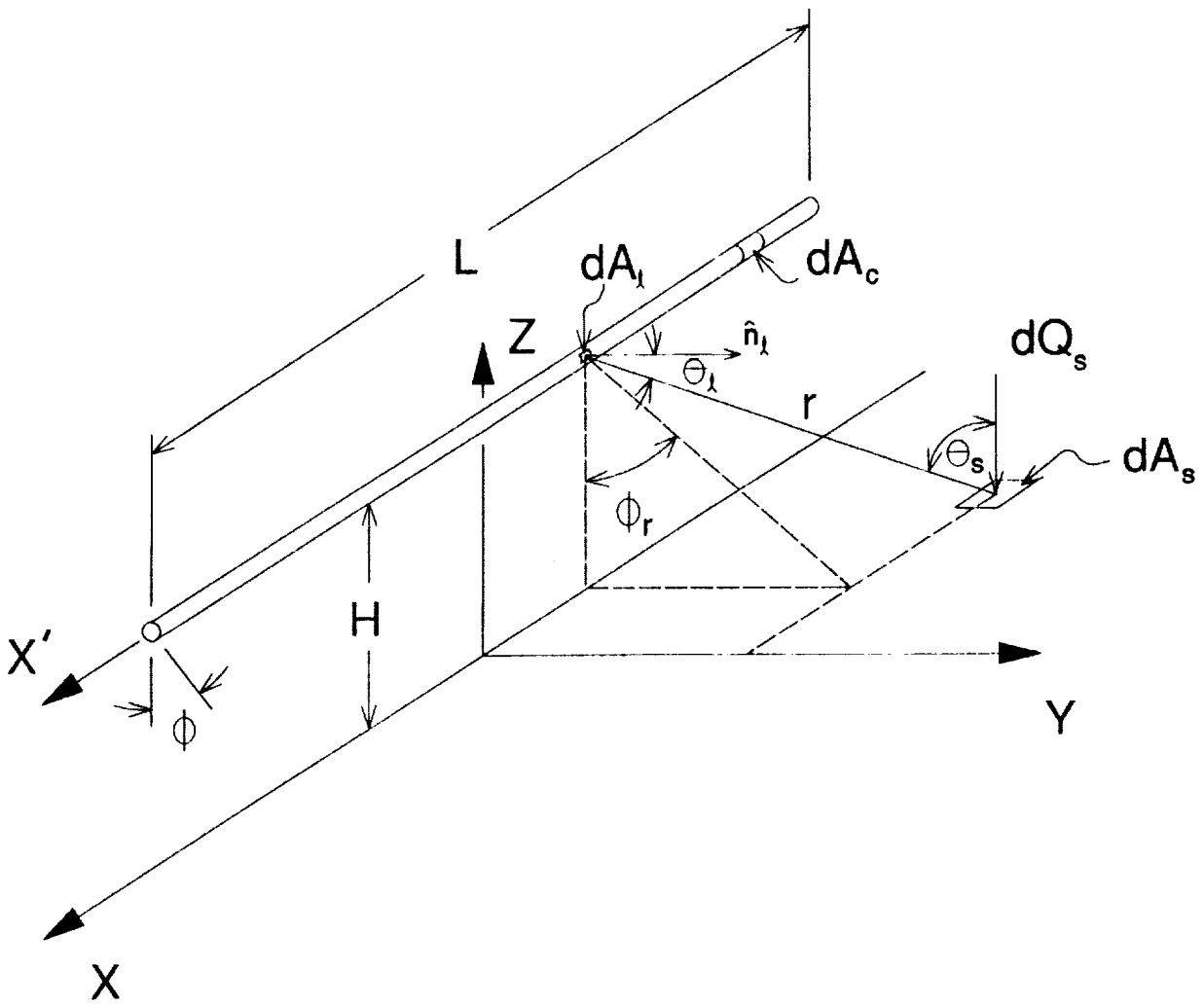
Figure 1.- Coordinates and dimensions for analysis of a cylindrical lamp.
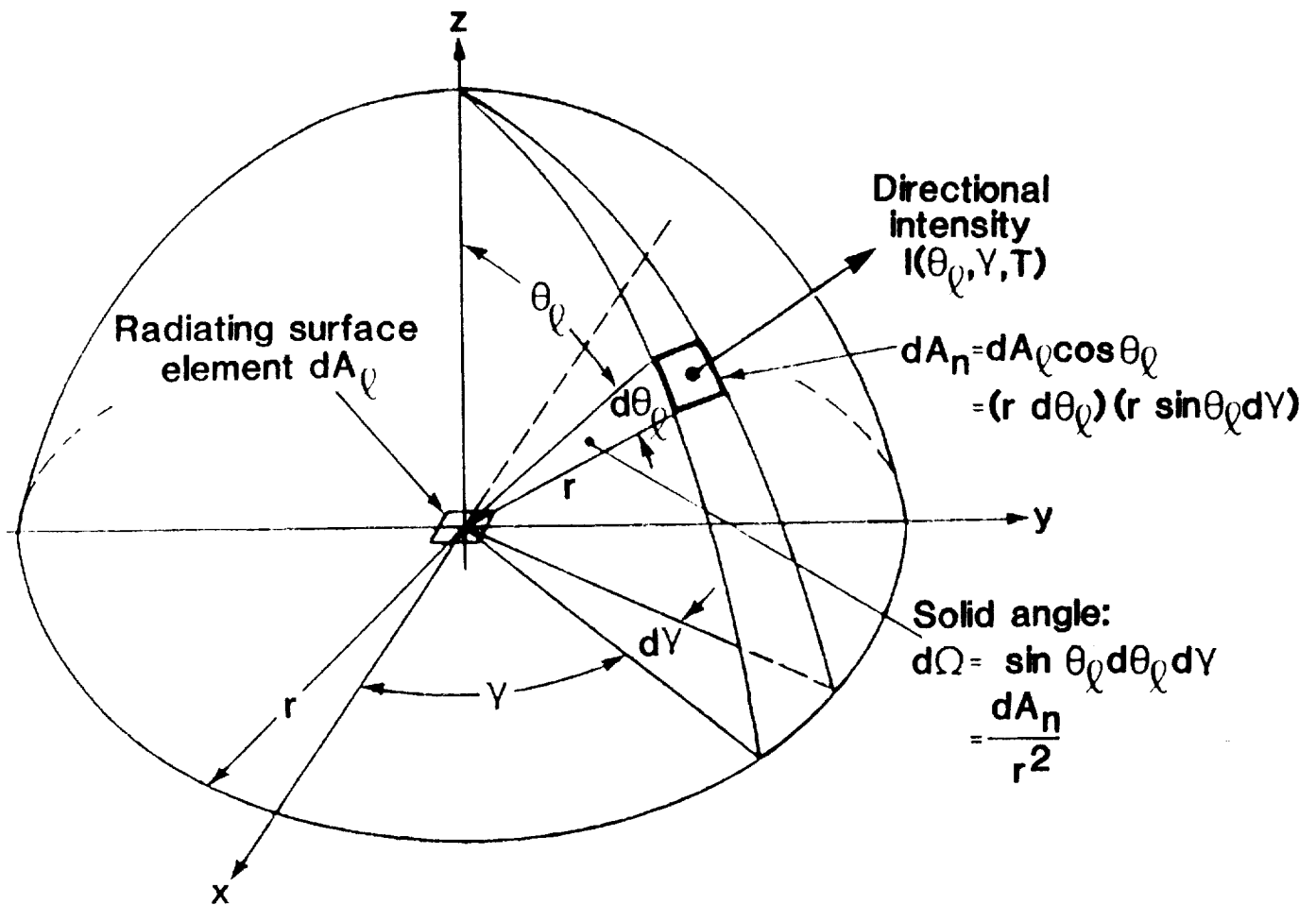
Figure 2.– Geometry and definitions associated with radiation to hemispherical space for a differential surface element.
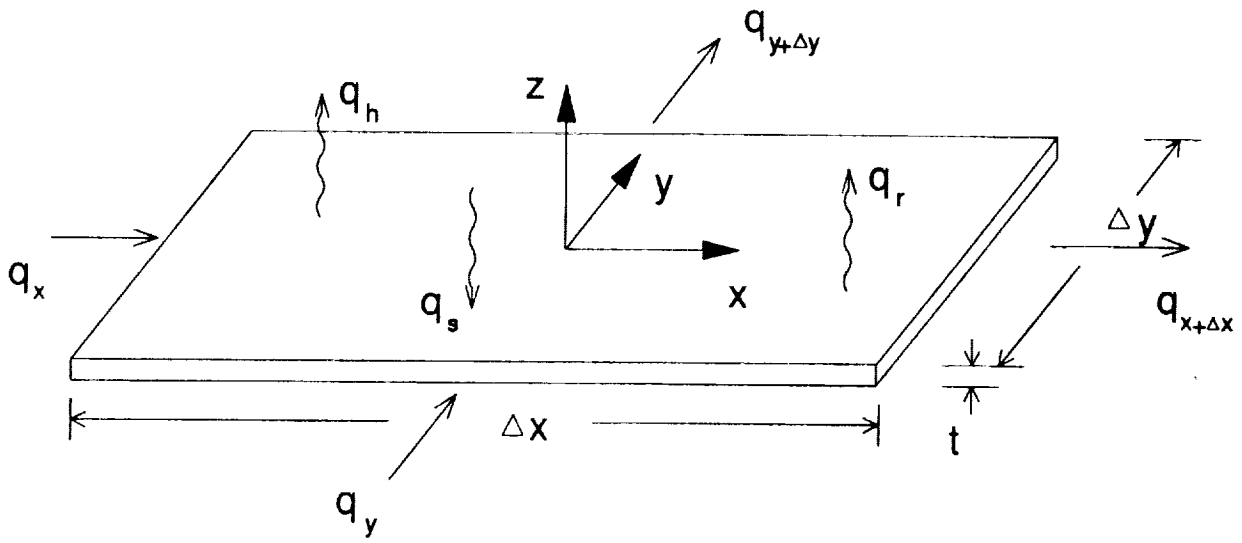
Figure 3.- Heat energy balance in a discrete portion of a thin plate.
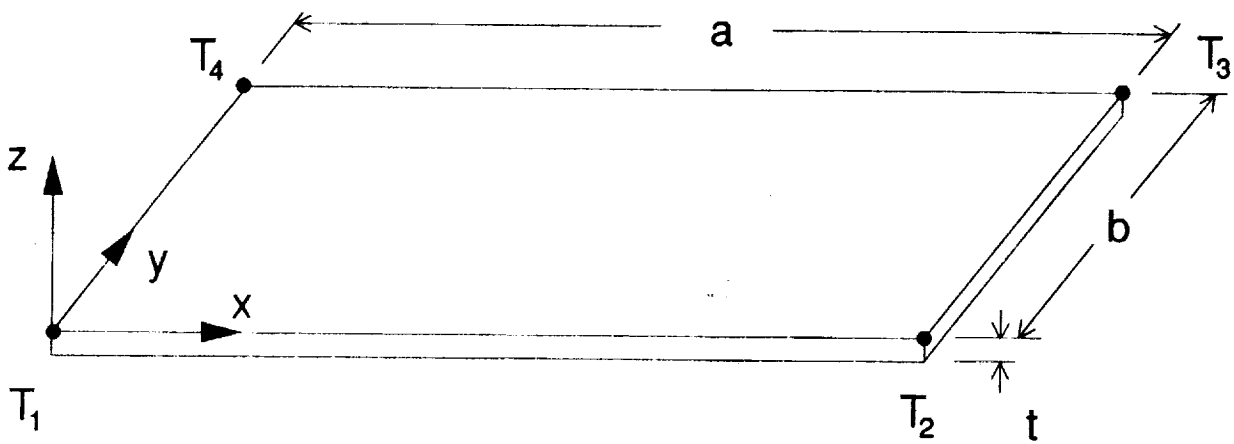
Figure 4.- Four noded rectangular thermal plate element.
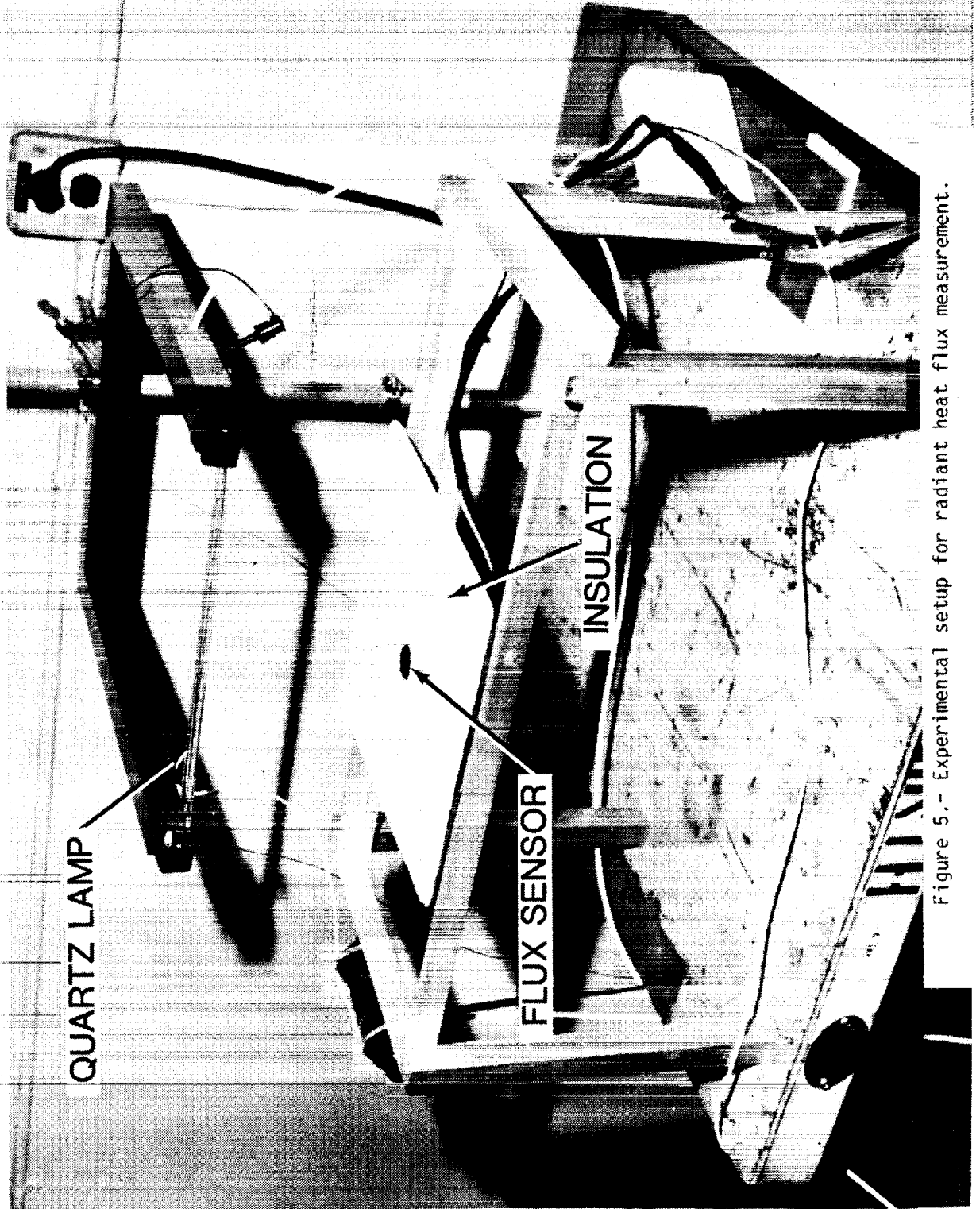
Figure 5.- Experimental setup for radiant heat flux measurement.

35
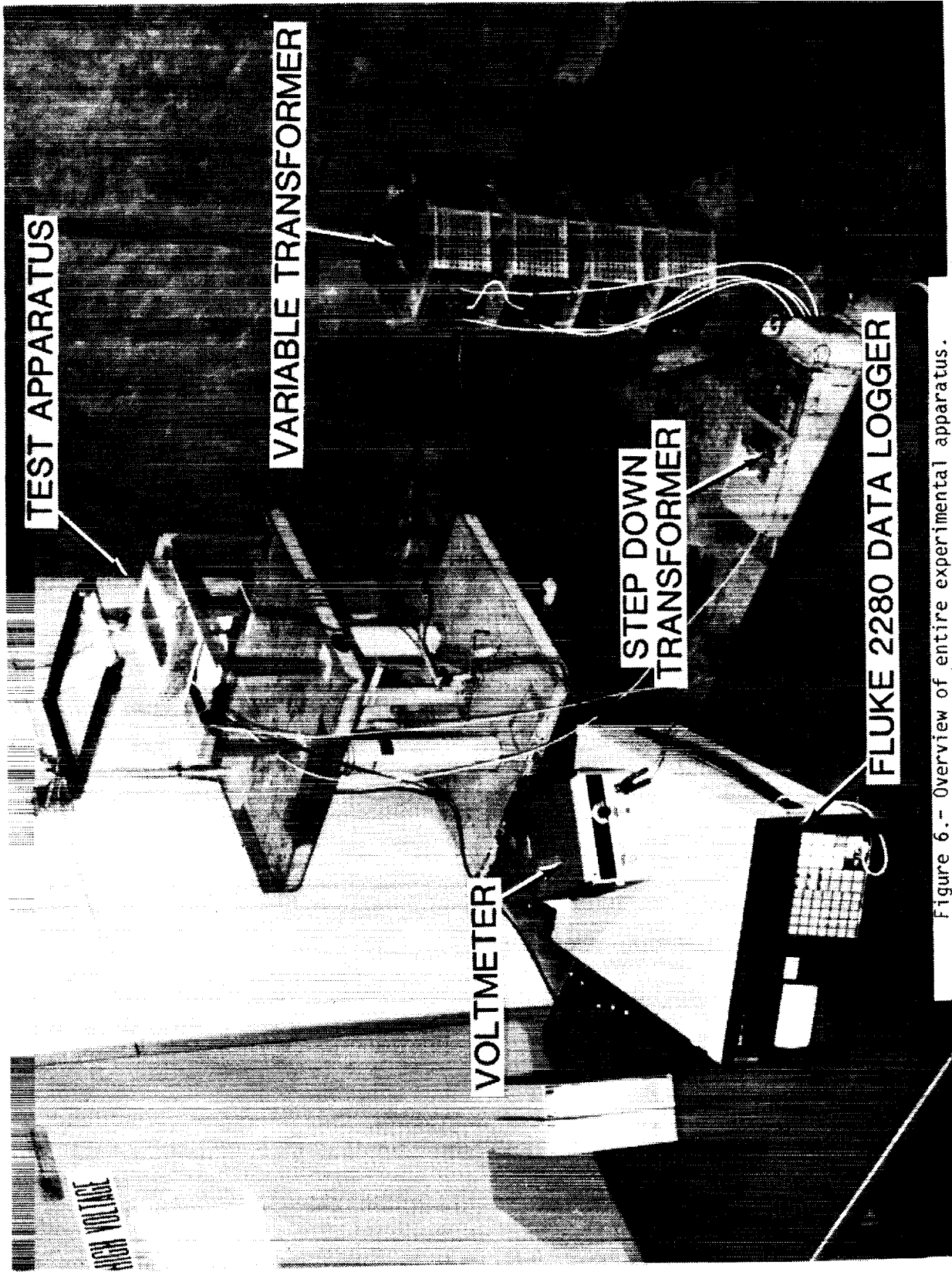
Figure 6.– Overview of entire experimental apparatus.

TEST APPARATUS

VARIABLE TRANSFORMER

STEP DOWN TRANSFORMER

FLUKE 2280 DATA LOGGER

VOLTMETER

HIGH VOLTAGE

36

SENSOR FOIL

SENSOR WIRES

ISOTHERMAL HEAT SINK
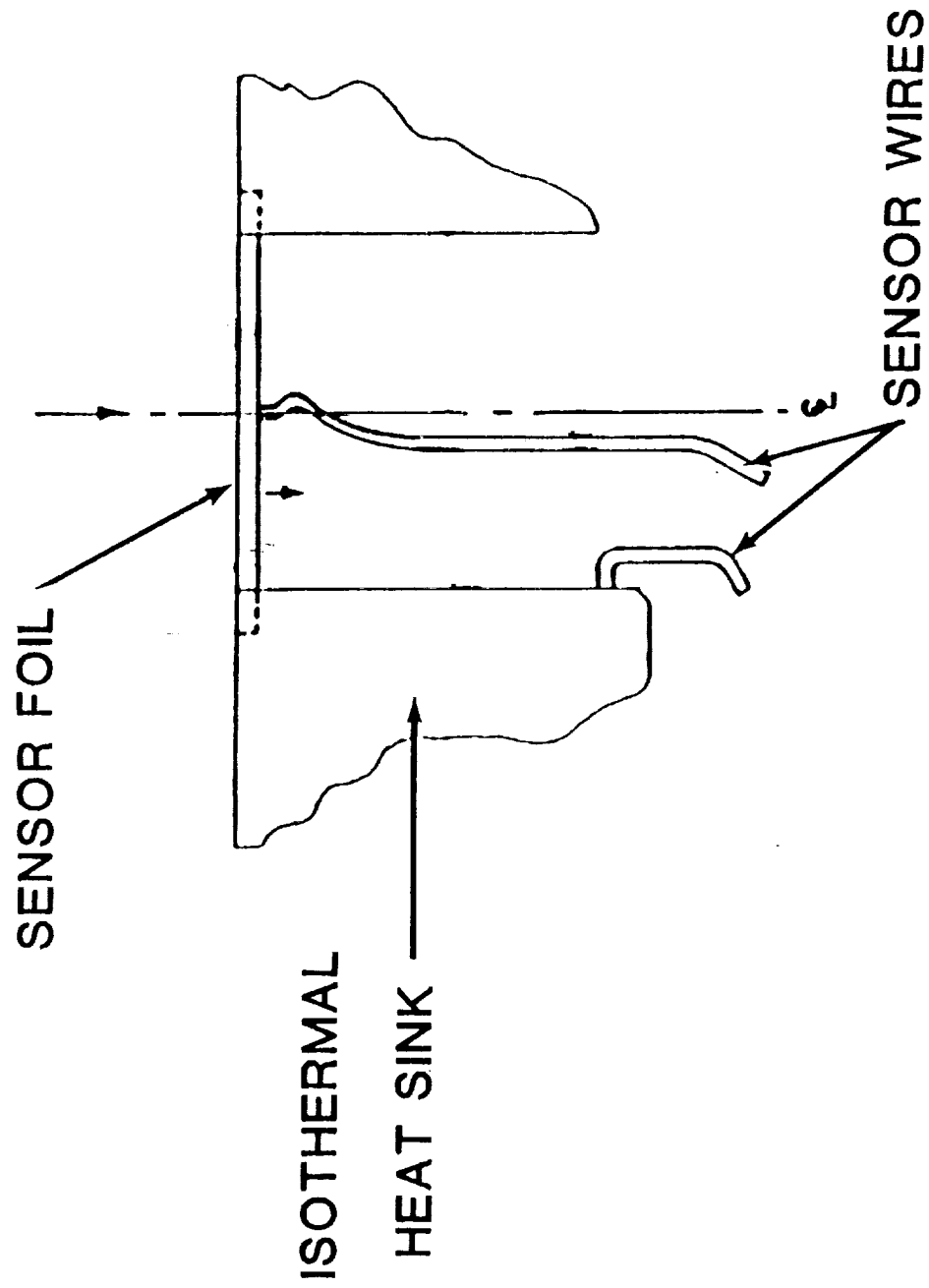
Figure 7.- Gardon-type heat flux sensor cross section and pertinent components.

QUARTZ LAMP

TEST SPECIMEN

INSULATION

THERMOCOUPLE LEADS
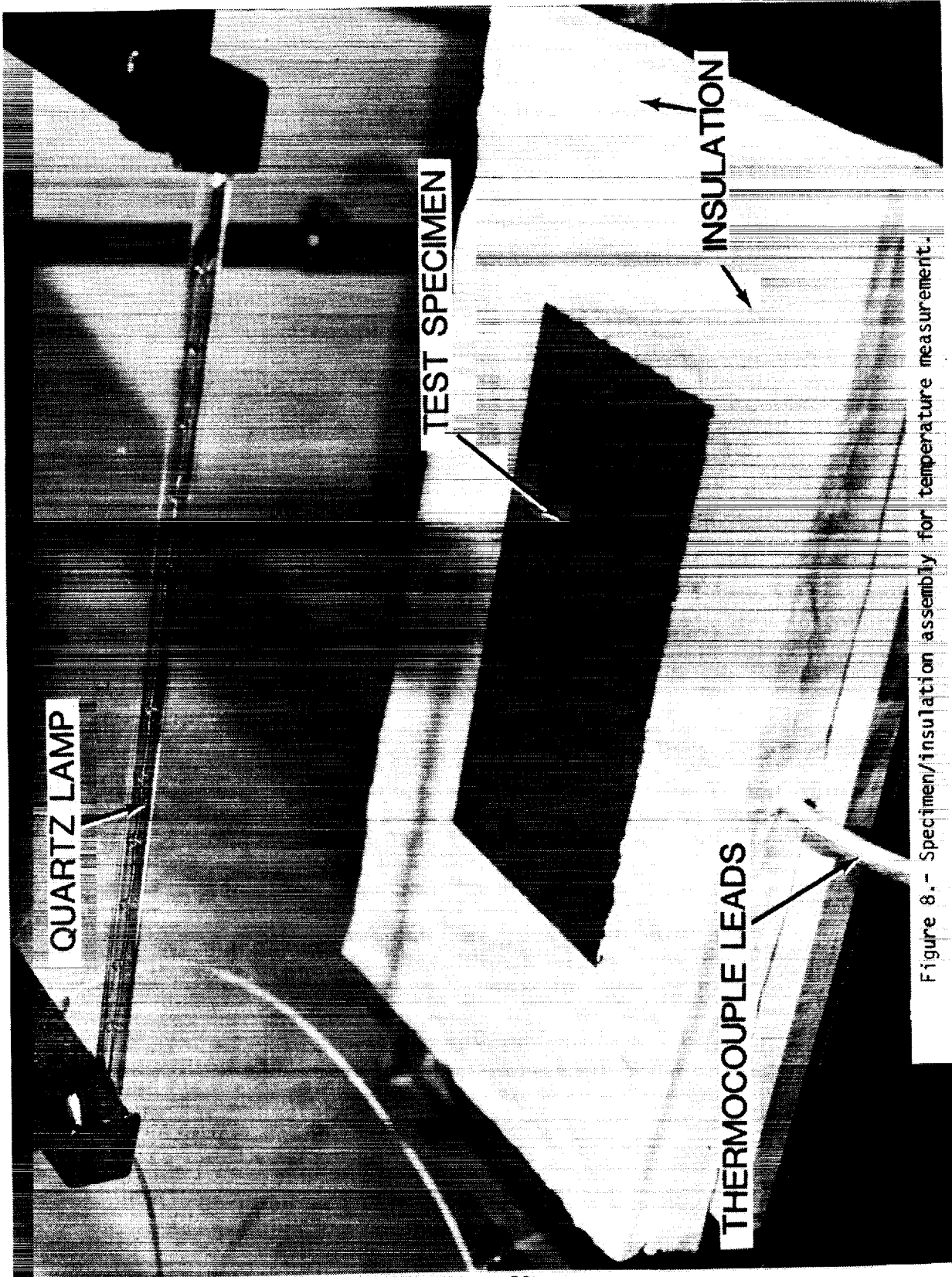
Figure 8.- Specimen/insulation assembly for temperature measurement.

38

AISI 347 STAINLESS STEEL
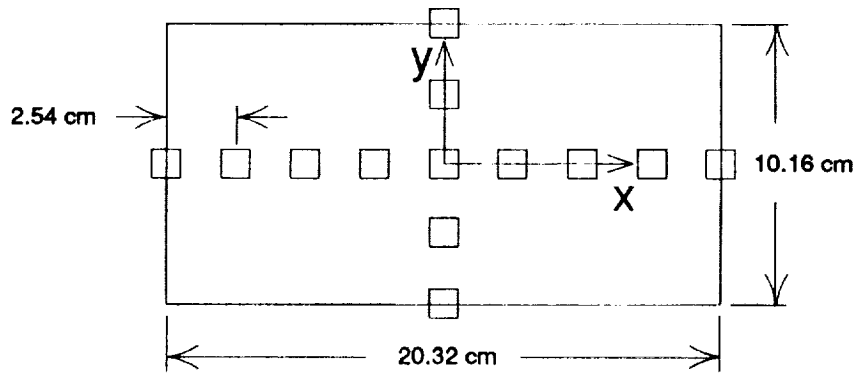
6Al-4V TITANIUM
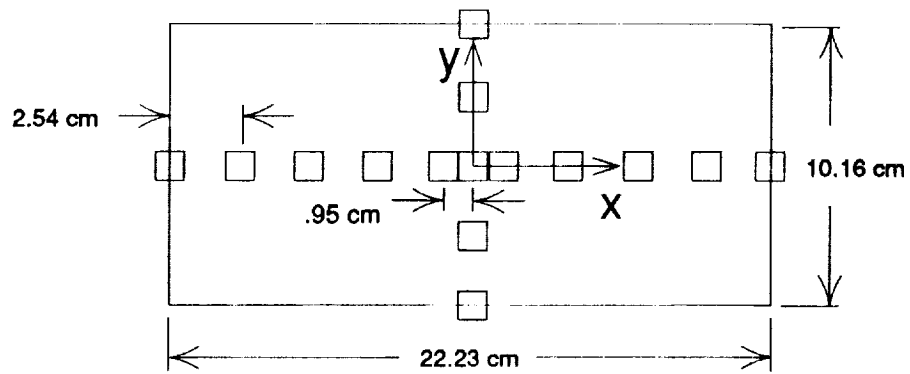
Figure 9.- Type-J thermocouple arrangement on the respective test specimens.
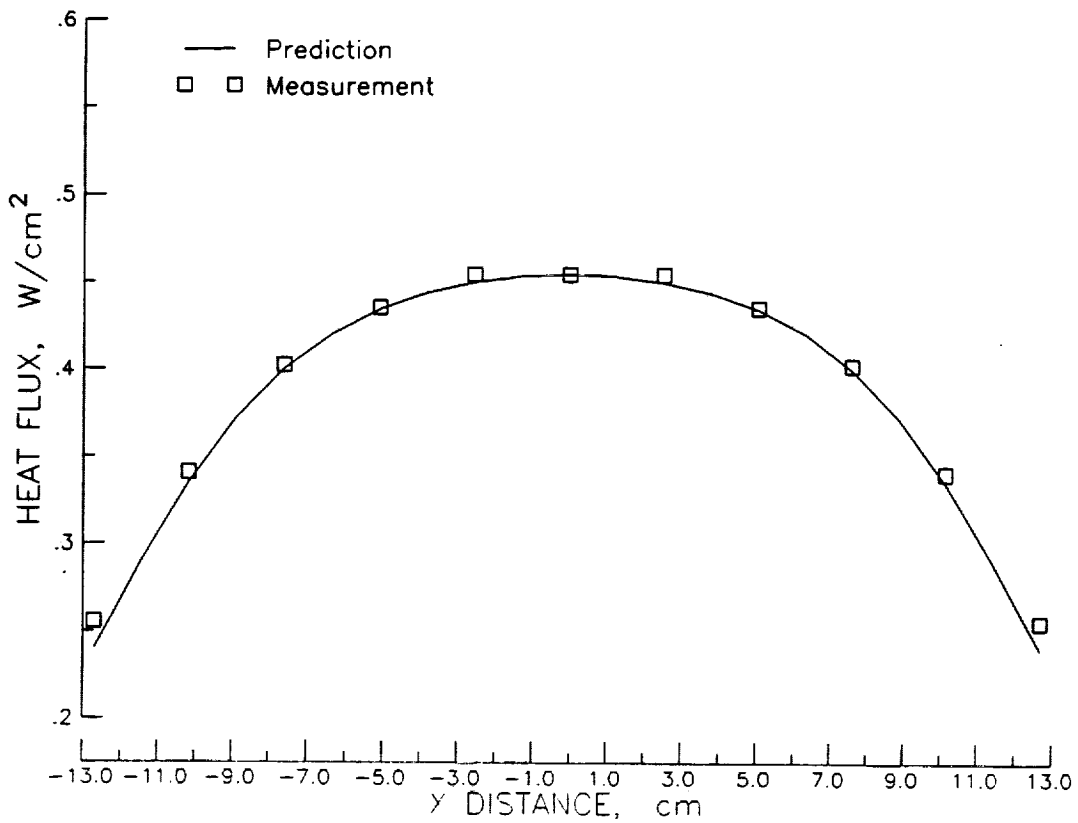
Figure 10.- Radiant heat flux distribution along the axis of the lamp for a
lamp-to-sensor distance of 15.24 cm and input voltage of 240 V.
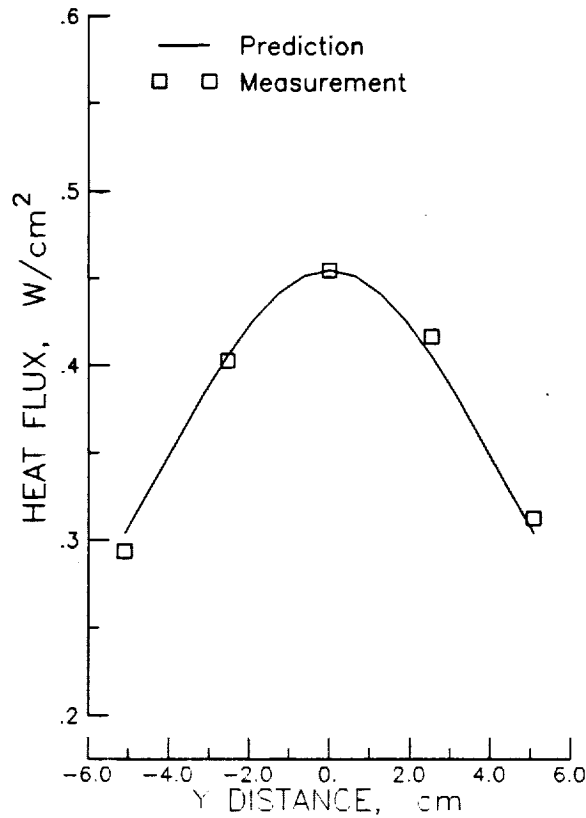
Figure 11.- Radiant heat flux distribution transverse to the lamp axis for a
lamp-to-sensor distance of 15.24 cm and input voltage of 240 V.
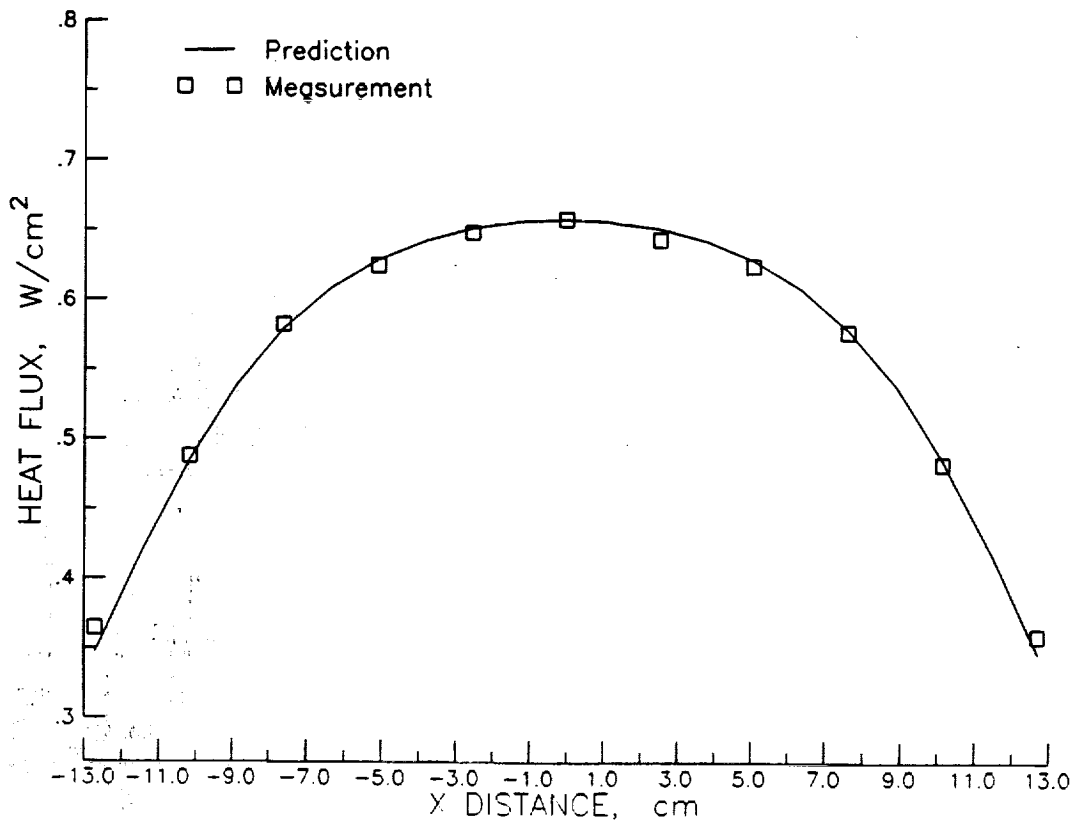
Figure 12.- Radiant heat flux distribution along the axis of the lamp for a lamp-to-sensor distance of 12.7 cm and input voltage of 240 V.
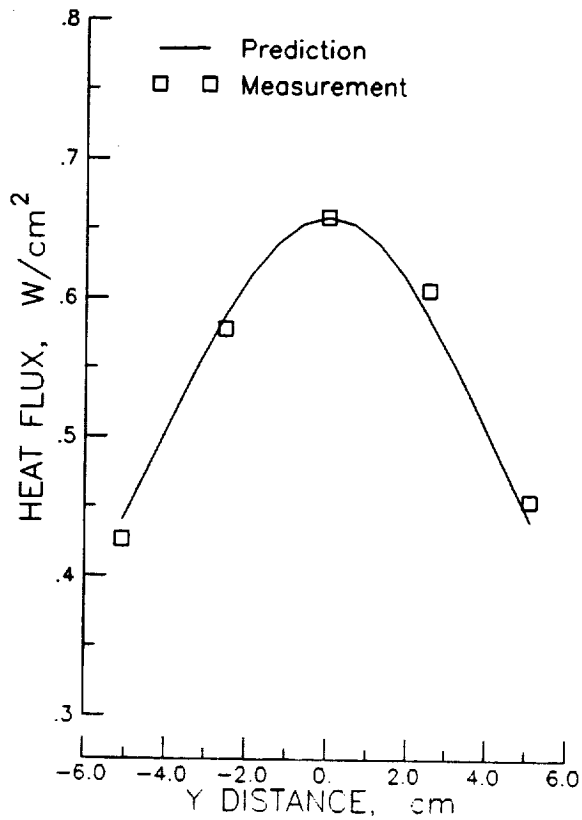
Figure 13.- Radiant heat flux distribution transverse to the lamp axis for a lamp-to-sensor distance of 12.7 cm and input voltage of 240 V.

41
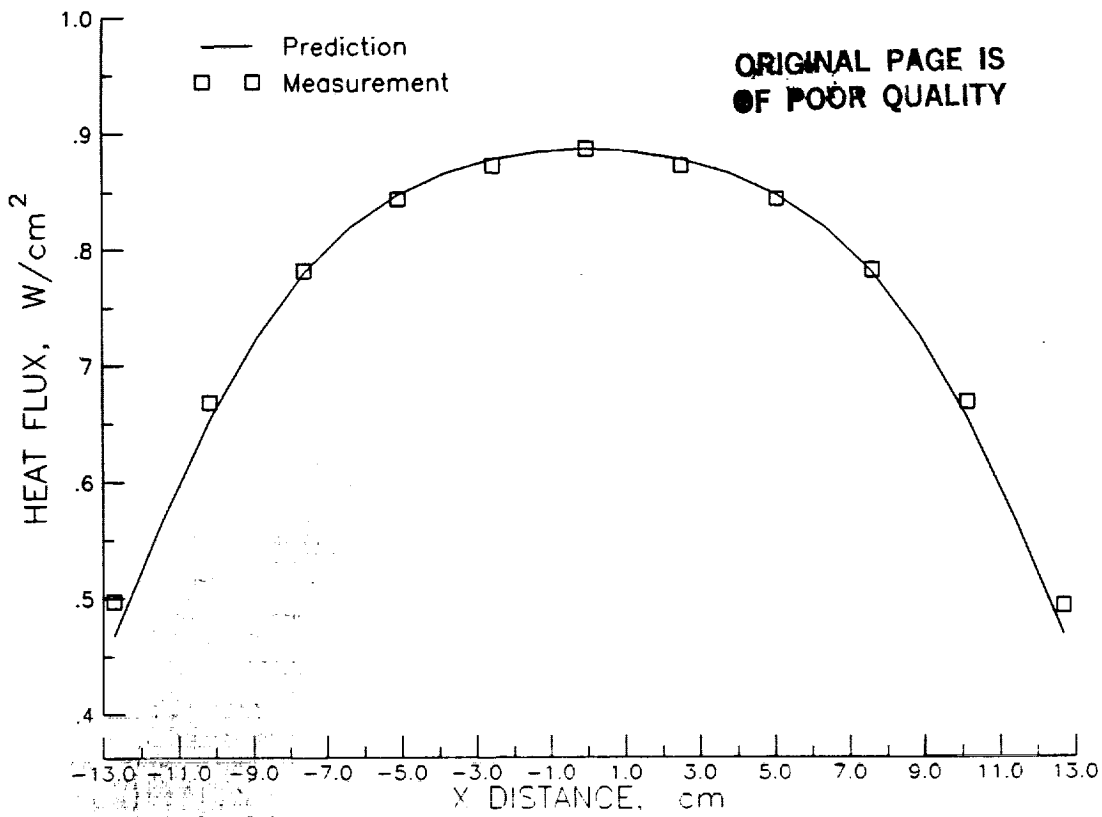
Figure 14.- Radiant heat flux distribution along the axis of the lamp for a lamp-to-sensor distance of 7.62 cm and input voltage of 240 V.
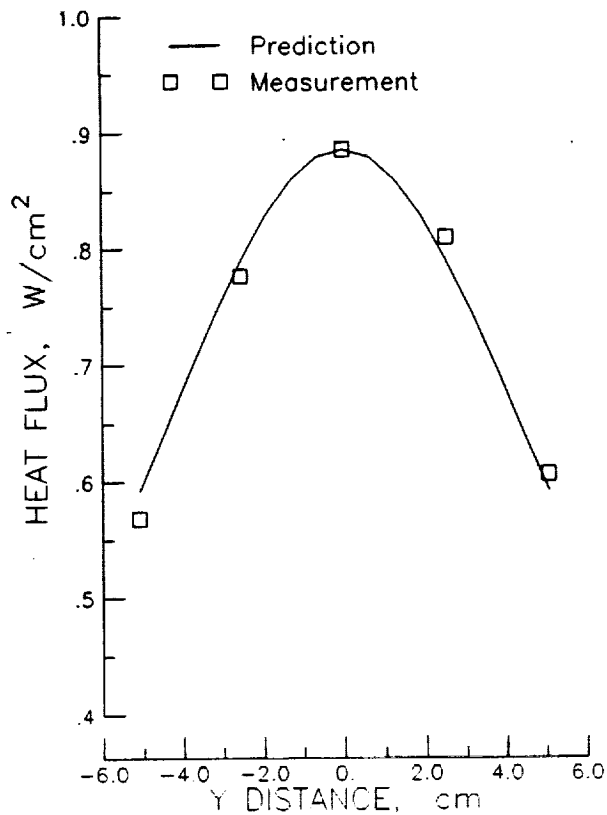
Figure 15.- Radiant heat flux distribution transverse to the lamp axis for a lamp-to-sensor distance of 7.62 cm and input voltage of 240 V.

42
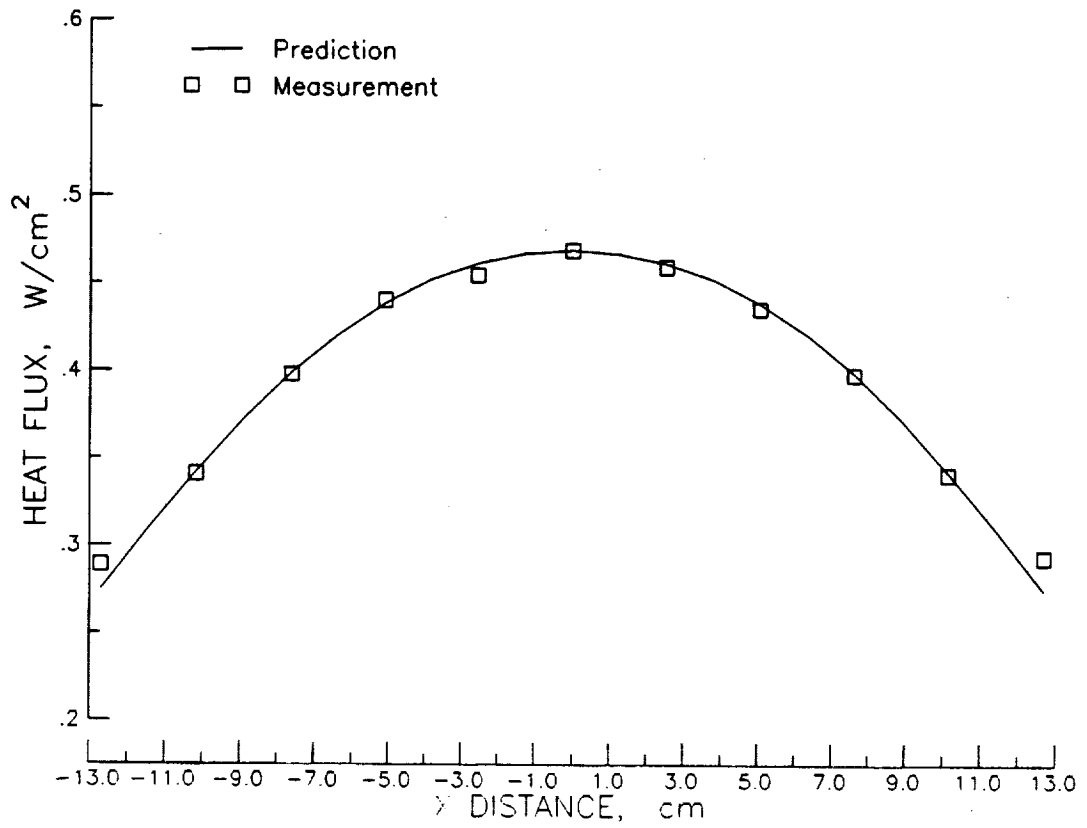
Figure 16.- Radiant heat flux distribution along the axis of the lamp for a lamp-to-sensor distance of 7.62 cm and input voltage of 200 V.
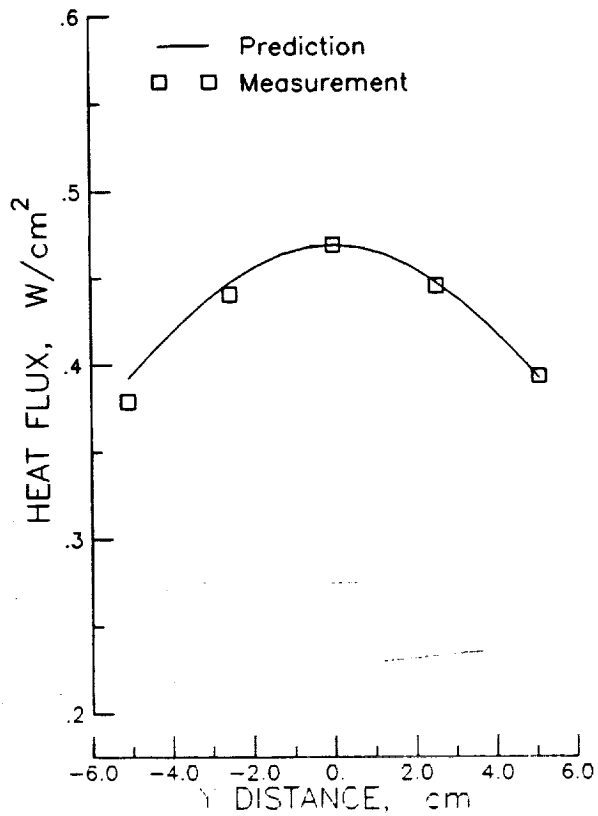
Figure 17.- Radiant heat flux distribution transverse to the lamp axis for a lamp-to-sensor distance of 7.62 cm and input voltage of 200 V.
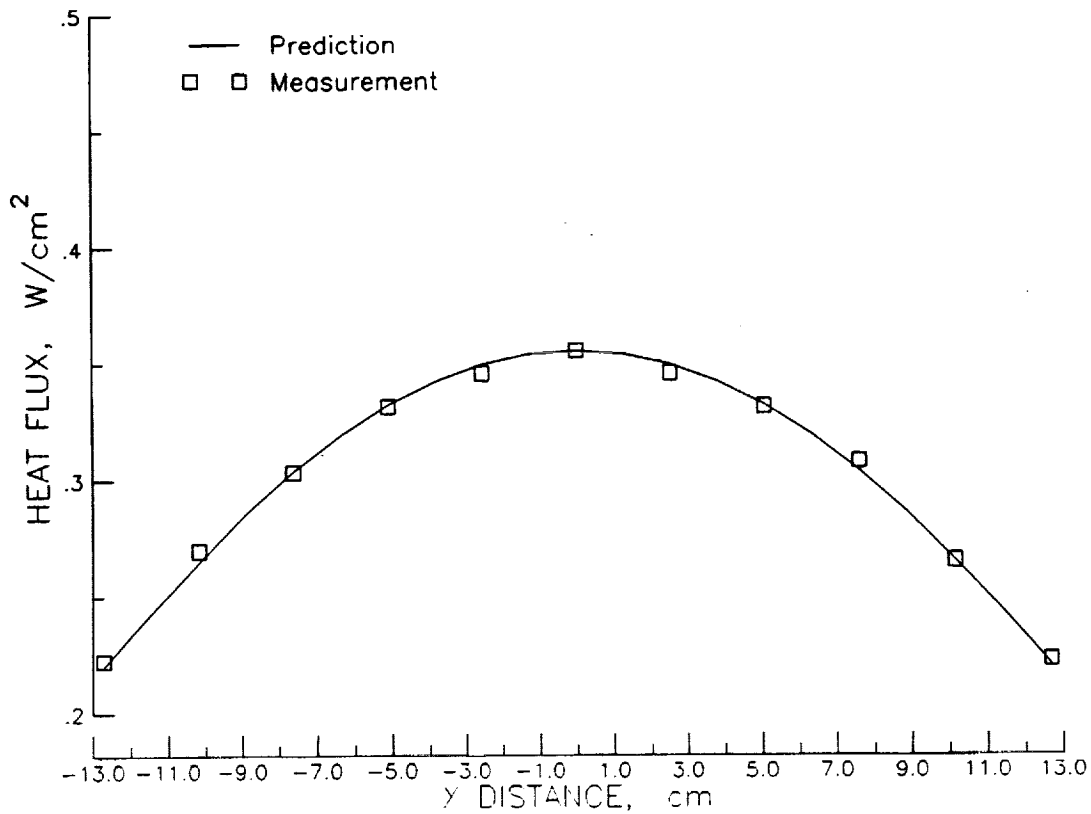
Figure 18.- Radiant heat flux distribution along the axis of the lamp for a lamp-to-sensor distance of 7.62 cm and input voltage of 160 V.
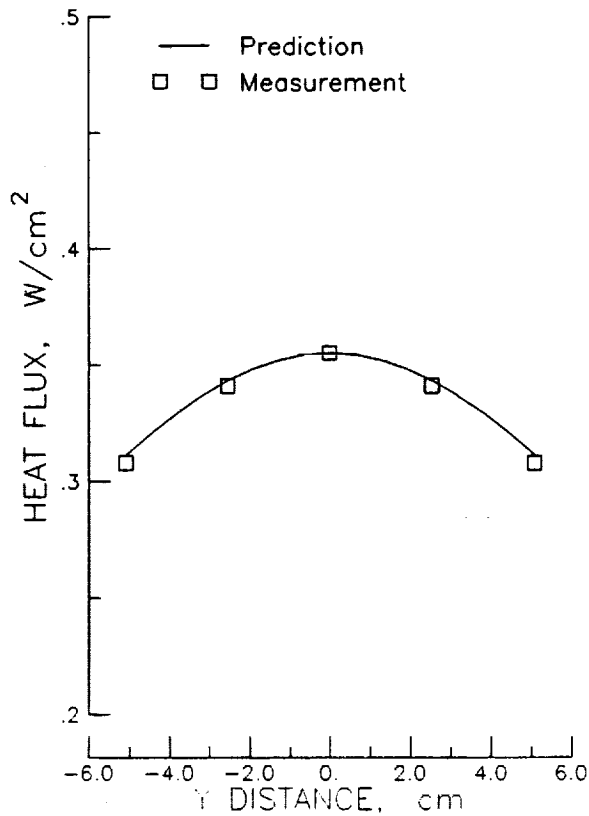
Figure 19.- Radiant heat flux distribution transverse to the lamp axis for a lamp-to-sensor distance of 7.62 cm and input voltage of 160 V.
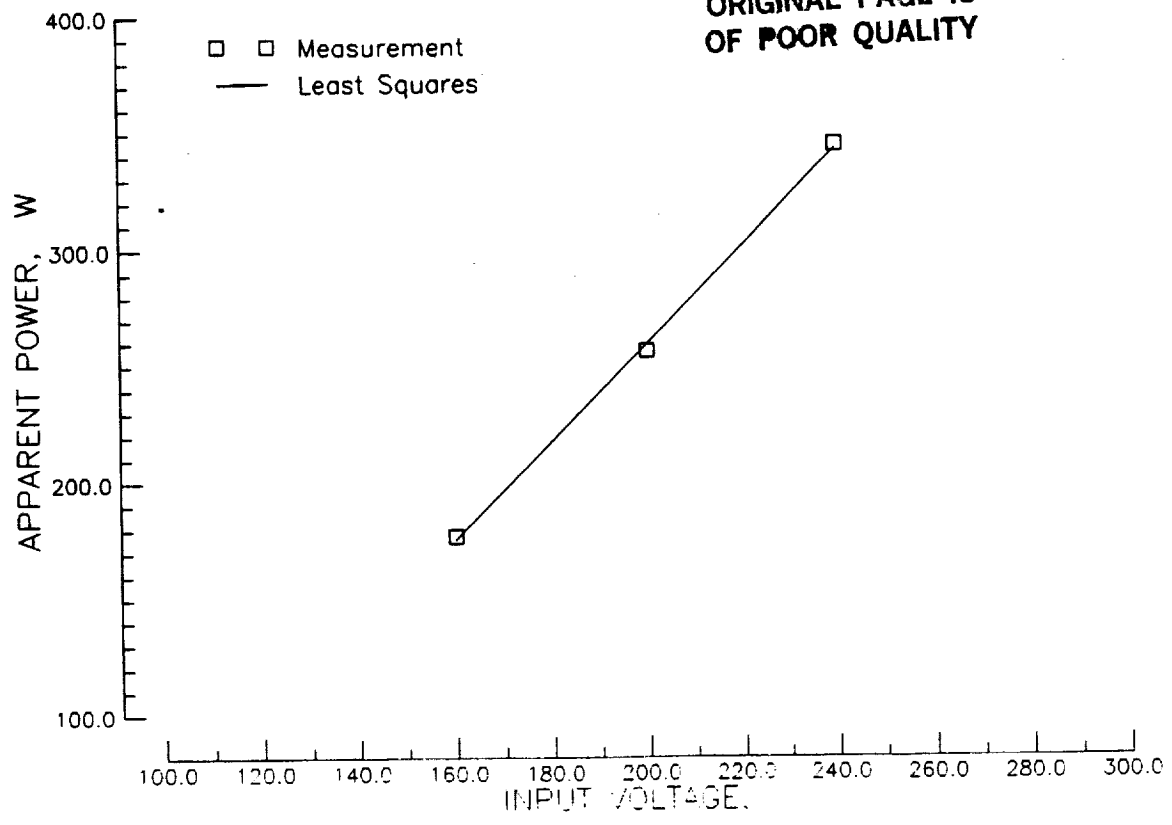
Figure 20.- Variation in apparent lamp power with an increasing input voltage for a lamp-to-sensor distance of 7.62 cm.
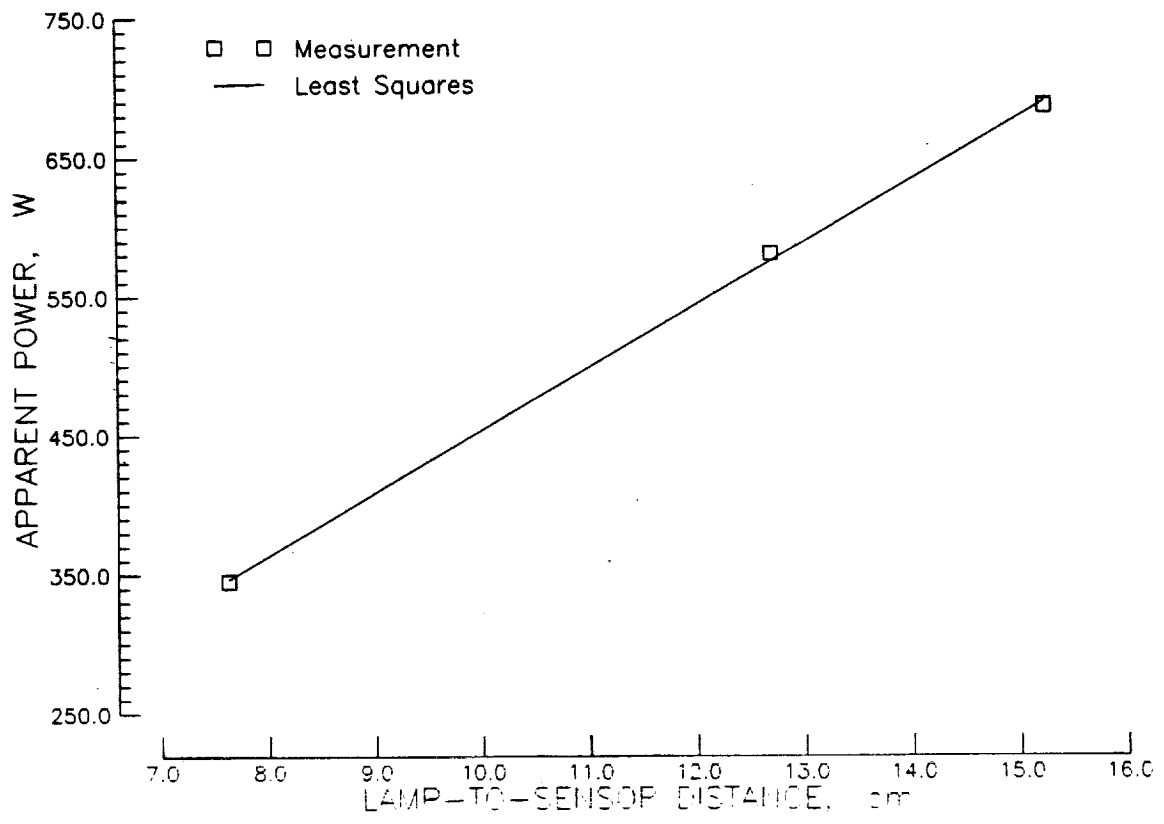
Figure 21.- Variation in apparent lamp power with an increasing lamp-to-sensor distance with a lamp input voltage of 240 V.
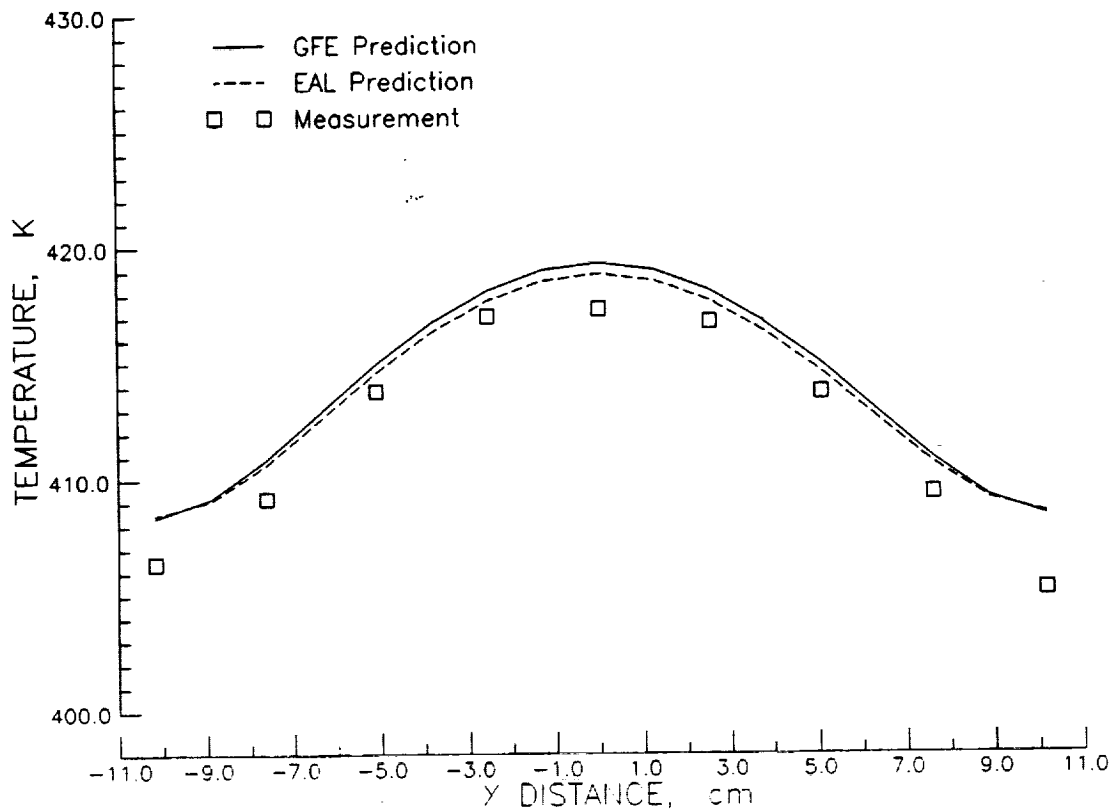
45
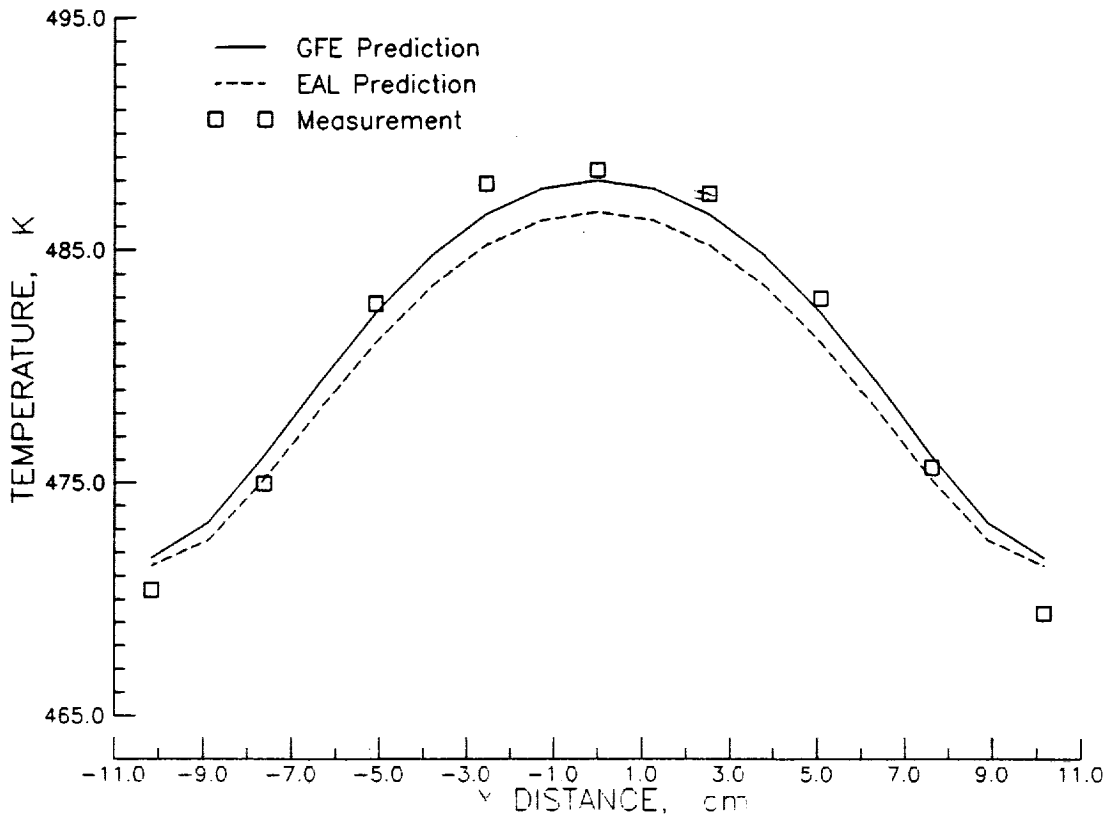
Figure 22.- Stainless steel specimen temperature distribution along the axis of the lamp for a lamp-to-panel distance of 7.62 cm.
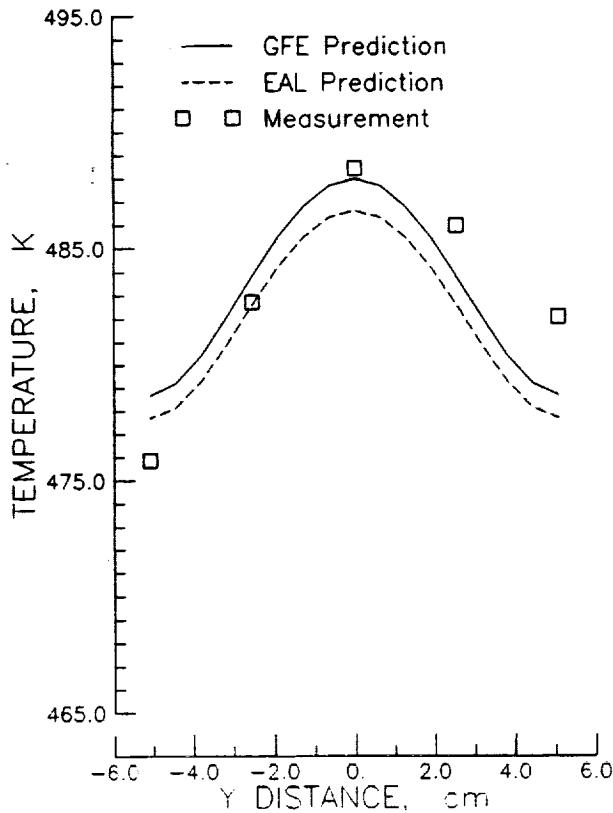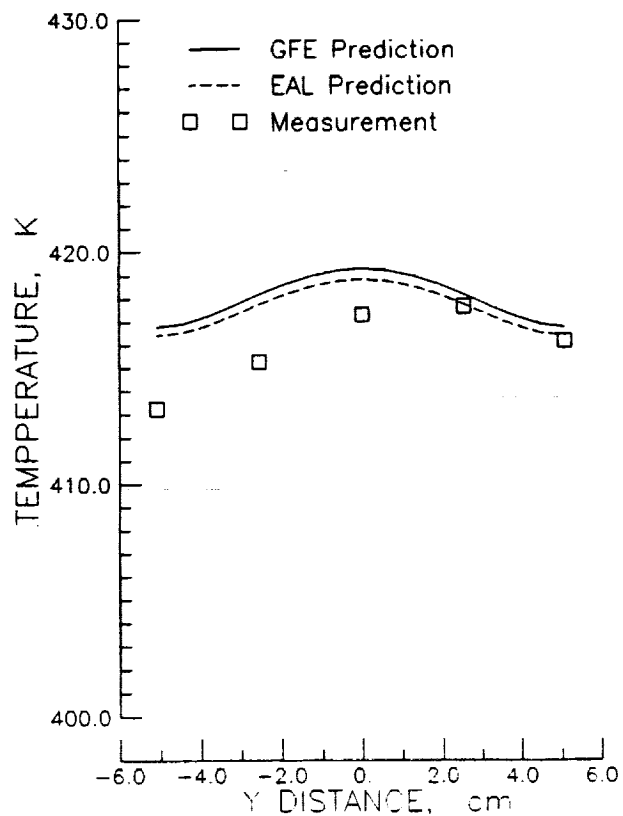

Figure 23.- Stainless steel specimen temperature distribution transverse to the axis of the lamp for a lamp-to-panel distance of 7.62 cm.
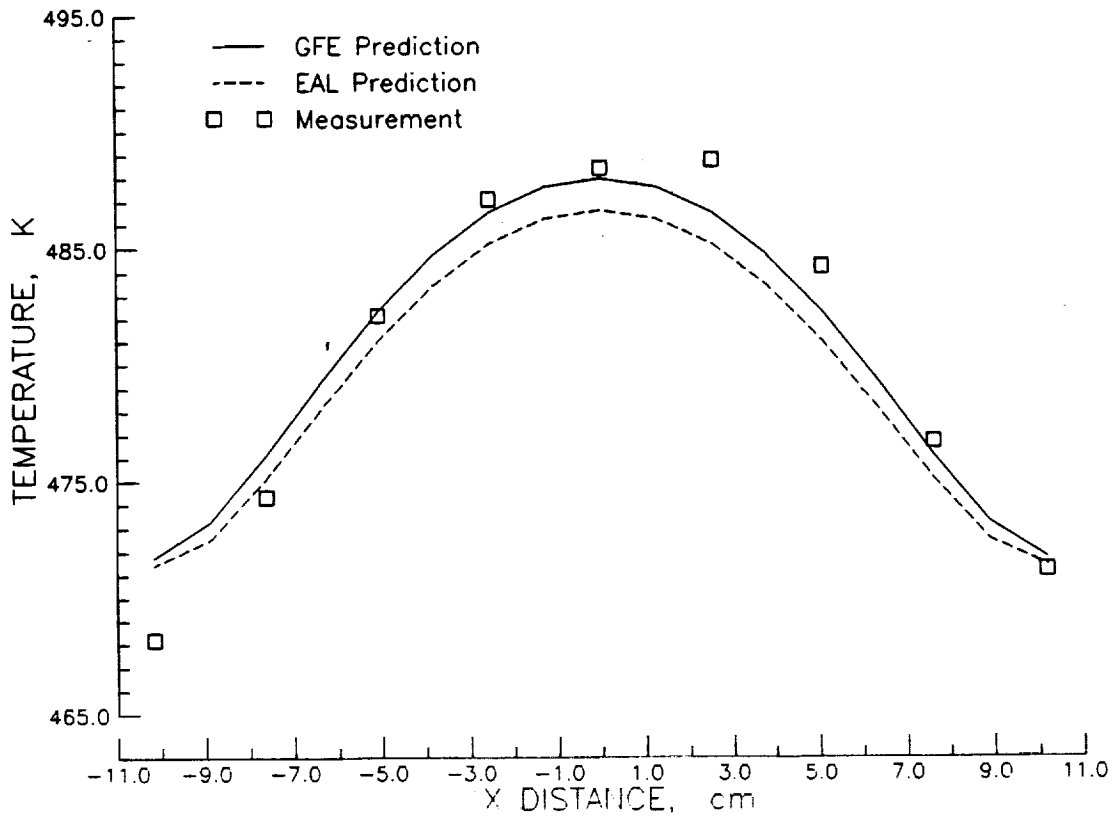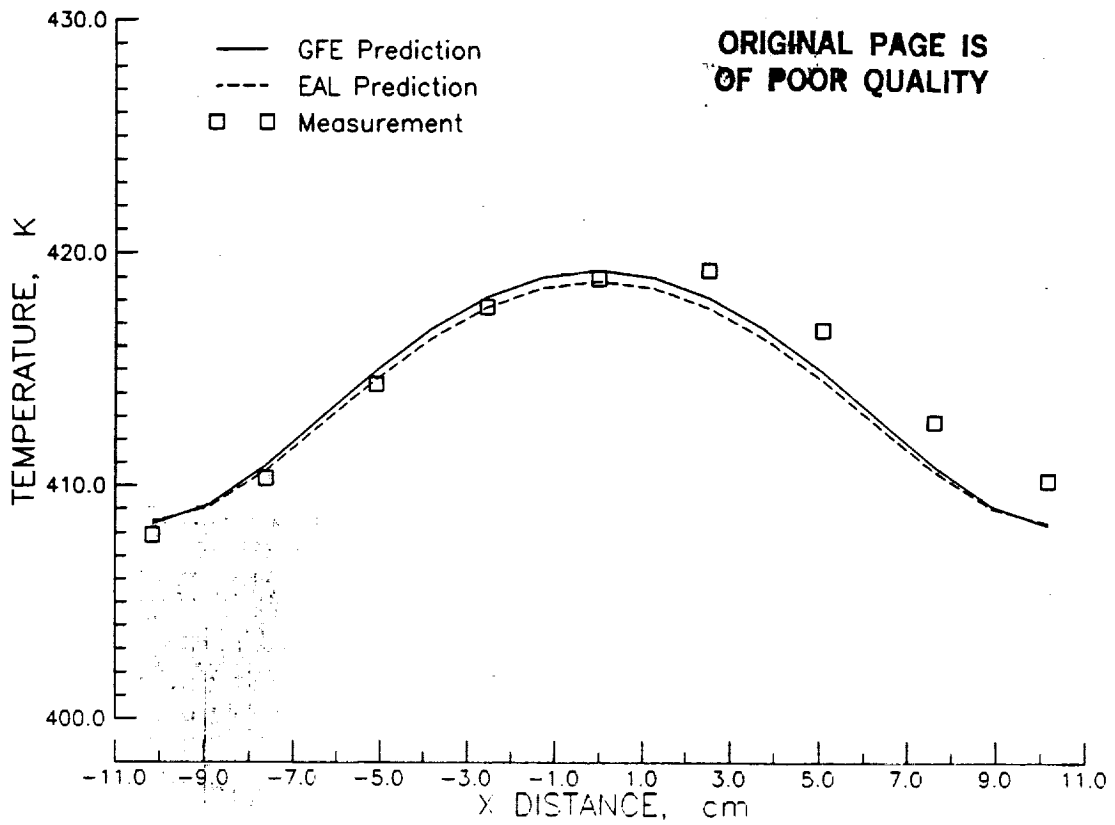
Figure 24.- Stainless steel specimen temperature distribution along the axis
of the lamp for a lamp-to-panel distance of 7.62 cm after specimen
rotation of 180° about the z-axis.
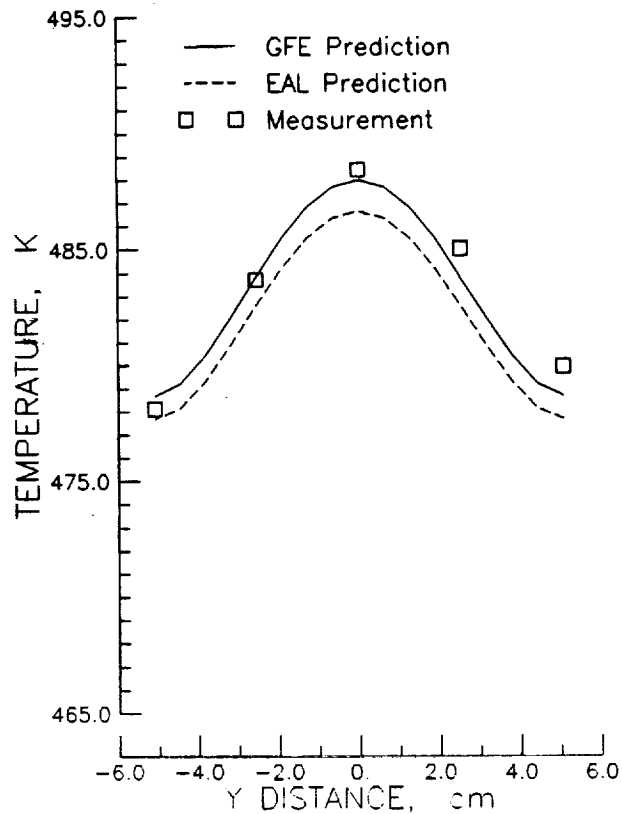
Figure 25.- Stainless steel specimen temperature distribution transverse
to the axis of the lamp for a lamp-to-panel distance of 7.62 cm
after specimen rotation of 180° about the z-axis.
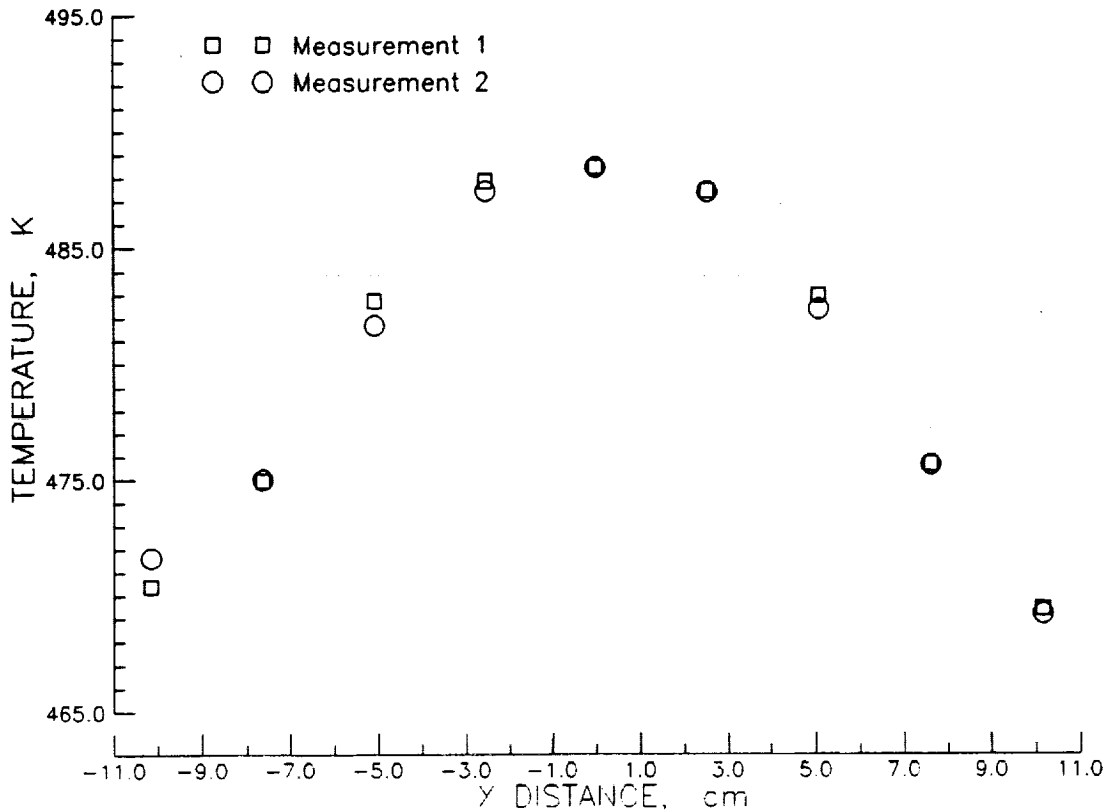
Figure 26.- Reproducibility comparison of the temperature distribution
along the lamp axis for two tests conducted at a lamp-to-panel
distance of 7.62 cm with the stainless steel specimen.
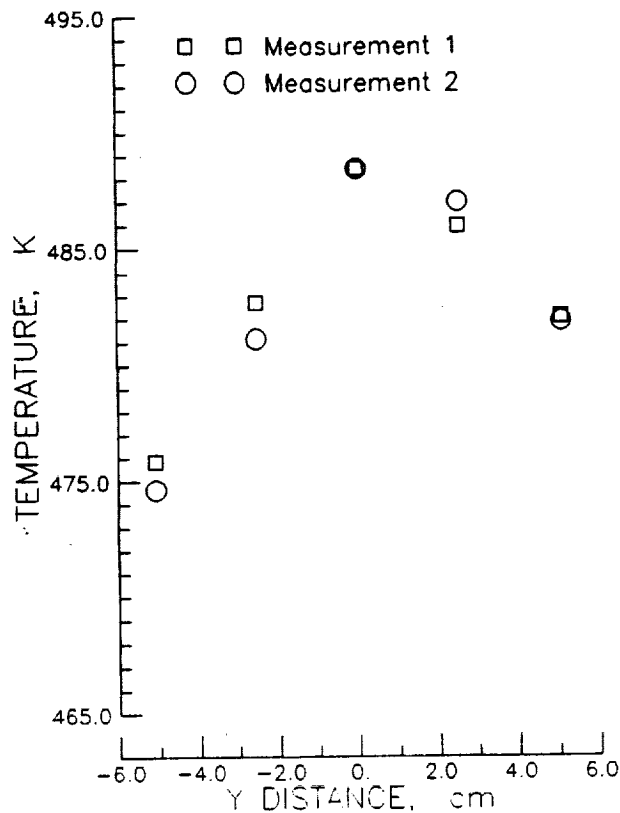
Figure 27.- Reproducibility comparison of the temperature distribution
transverse to the lamp axis for two tests conducted at a lamp-
to-panel distance of 7.62 cm with the stainless steel specimen.
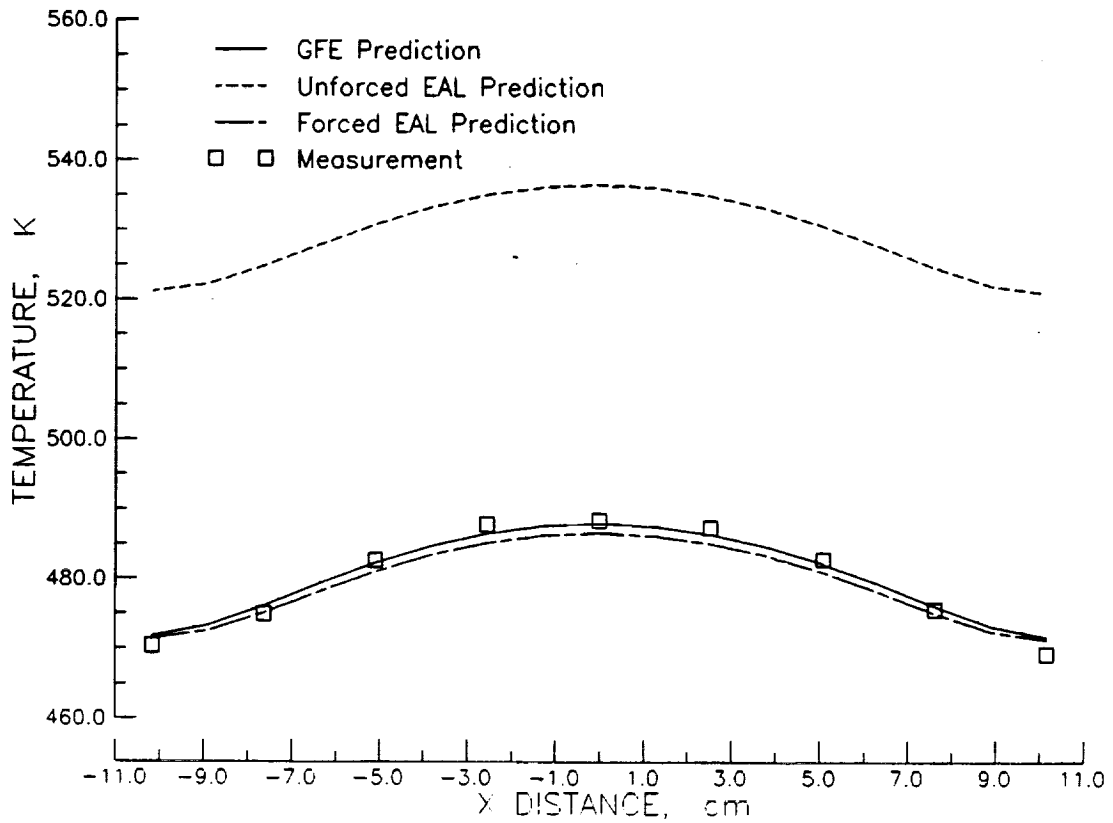
Figure 28.- Comparison of the results shown in figure 19 with a prediction made by EAL while allowing it to choose free convection correlation parameters.
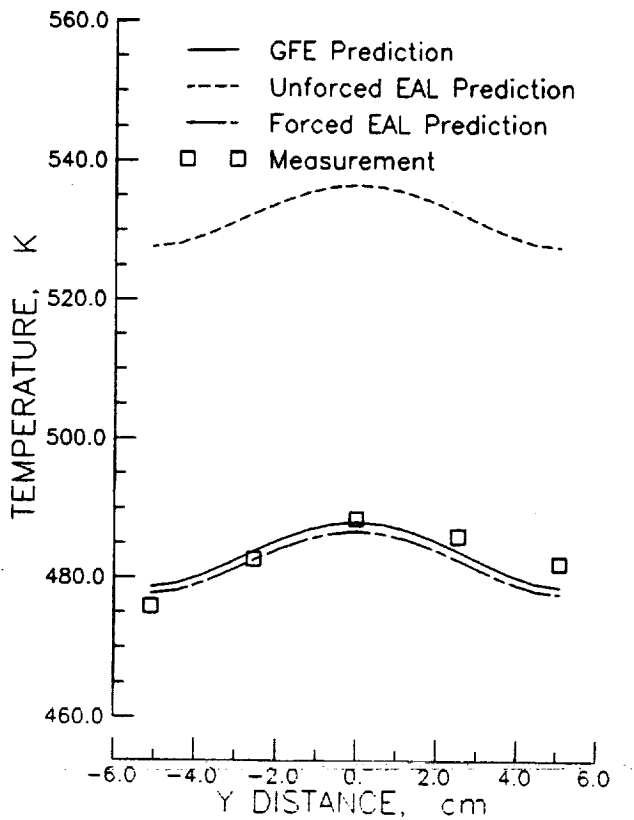
Figure 29.- Comparison of the results shown in figure 20 with a prediction made by EAL while allowing it to choose free convection correlation parameters.

Figure 30.- Stainless steel specimen temperature distribution along the axis of the lamp for a lamp-to-panel distance of 12.7 cm.
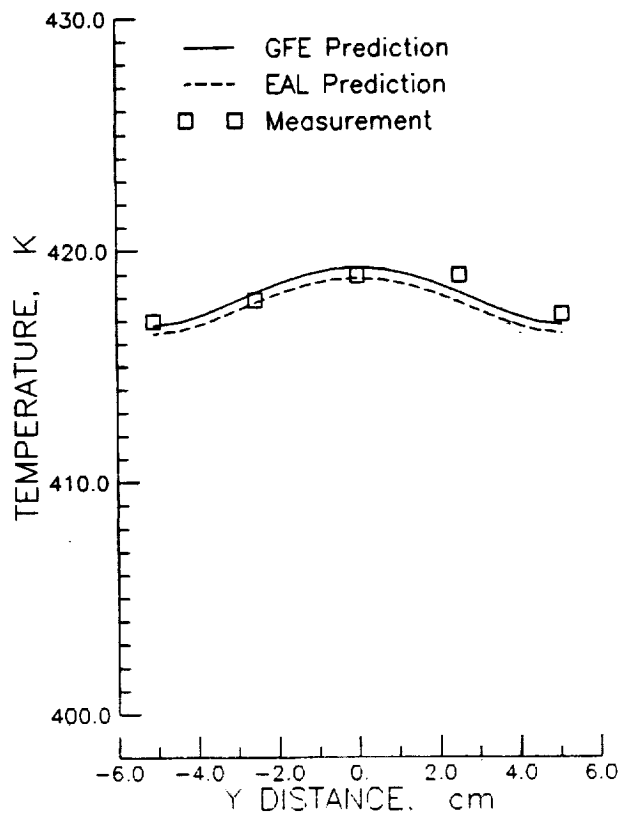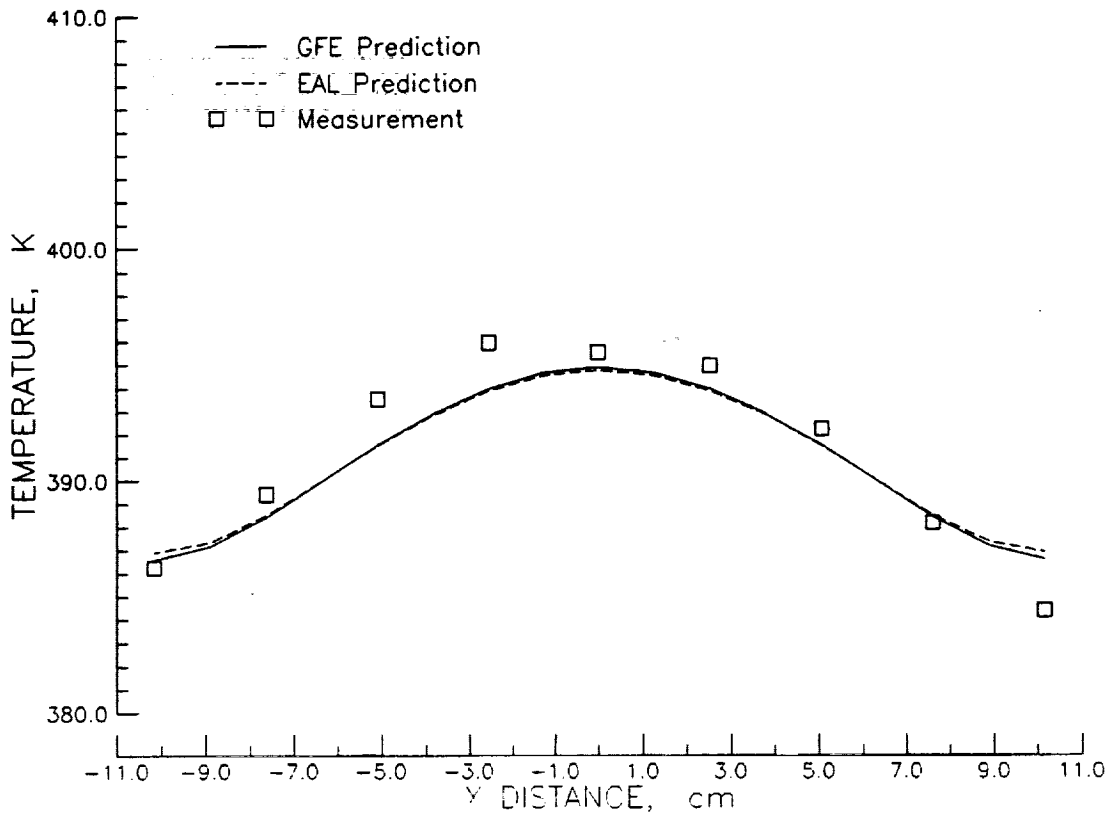

Figure 31.- Stainless steel specimen temperature distribution transverse to the axis of the lamp for a lamp-to-panel distance of 12.7 cm.

Figure 32.- Stainless steel specimen temperature distribution along the axis of the lamp for a lamp-to-panel distance of 12.7 cm after specimen rotation of 180° about the z-axis.

Figure 33.- Stainless steel specimen temperature distribution transverse to the axis of the lamp for a lamp-to-panel distance of 12.7 cm after specimen rotation of 180° about the z-axis.

51

Figure 34.- Stainless steel specimen temperature distribution along the axis of the lamp for a lamp-to-panel distance of 15.24 cm.
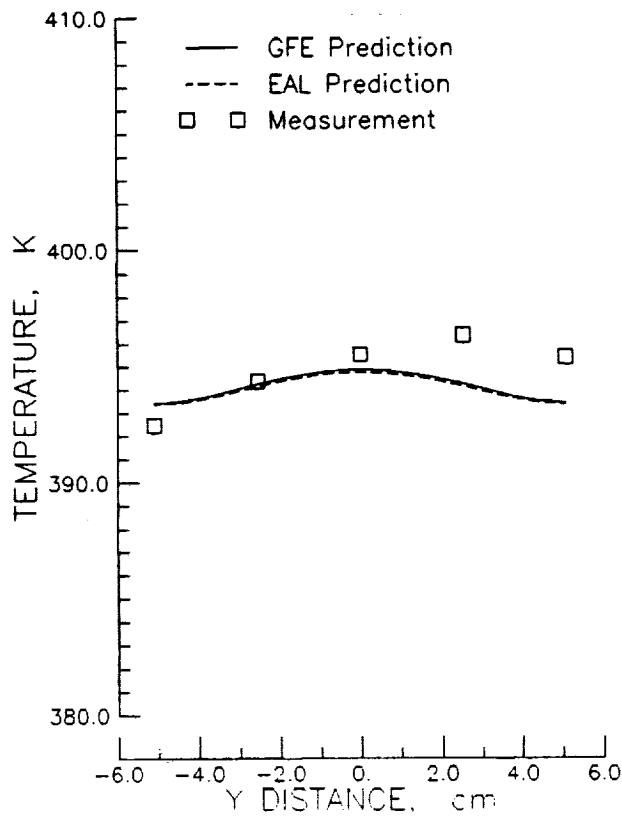

Figure 35.- Stainless steel specimen temperature distribution transverse to the axis of the lamp for a lamp-to-panel distance of 15.24 cm.
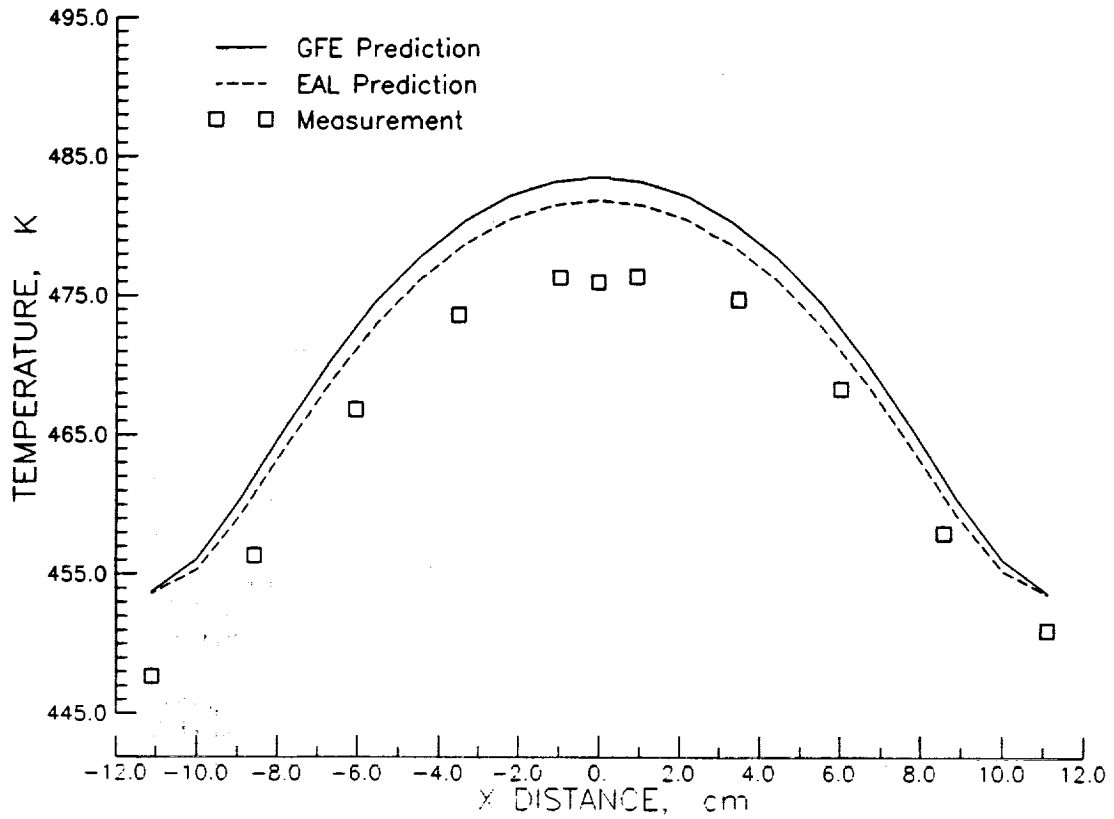
Figure 36.- Titanium specimen temperature distribution along the axis of the lamp for a lamp-to-panel distance of 7.62 cm.
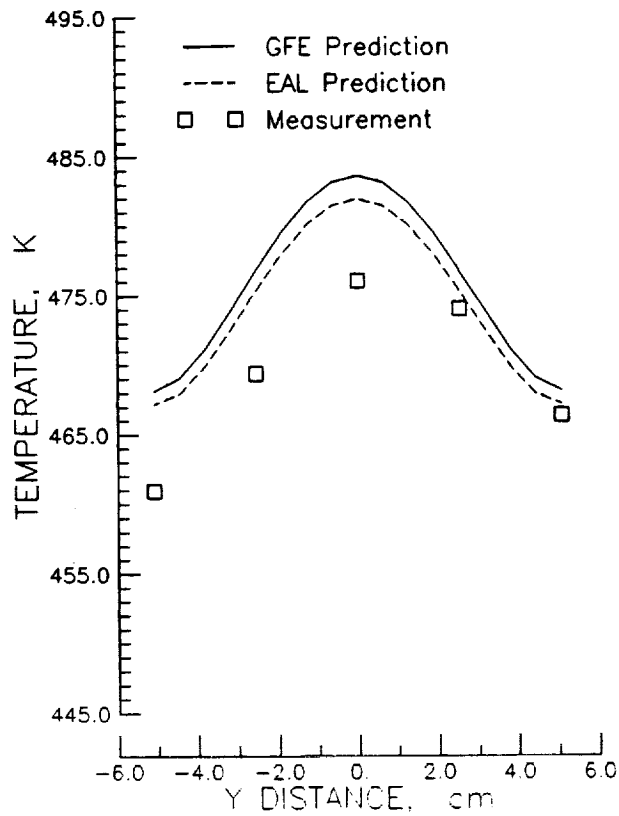

Figure 37.- Titanium specimen temperature distribution transverse to the axis of the lamp for a lamp-to-panel distance of 7.62 cm.
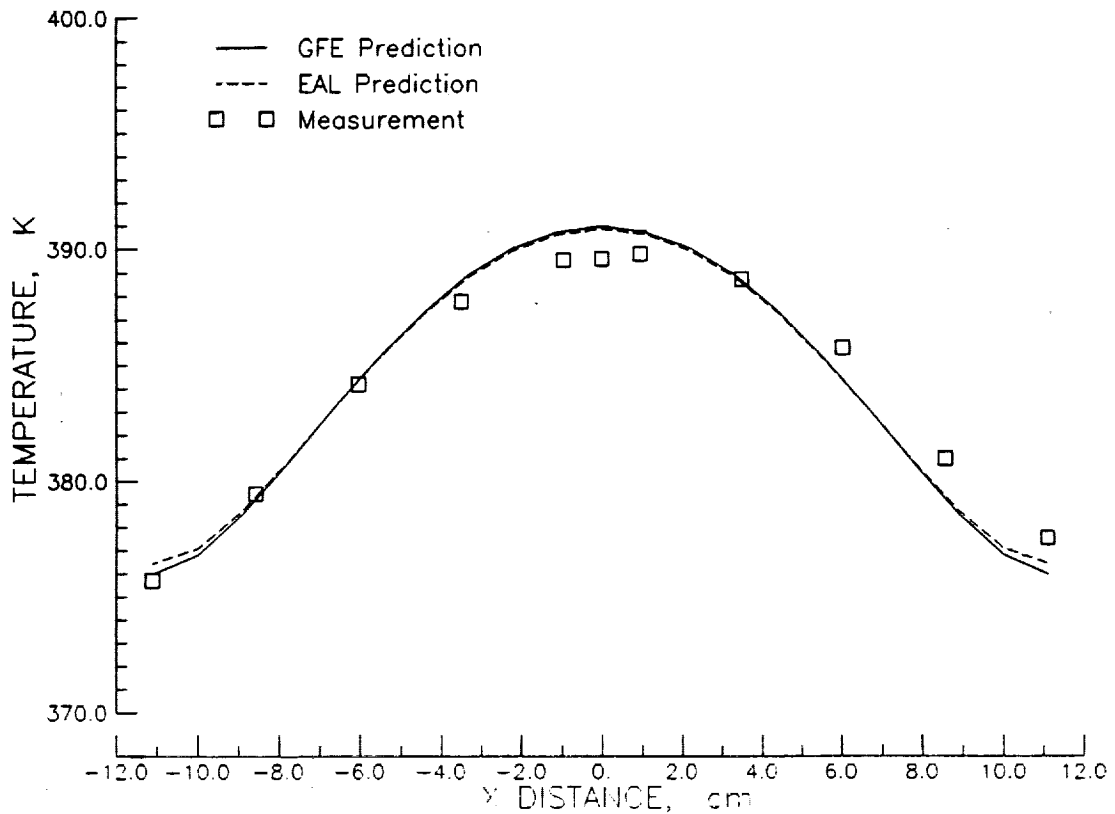
Figure 38.- Titanium specimen temperature distribution along the axis of the lamp for a lamp-to-panel distance of 15.24 cm.
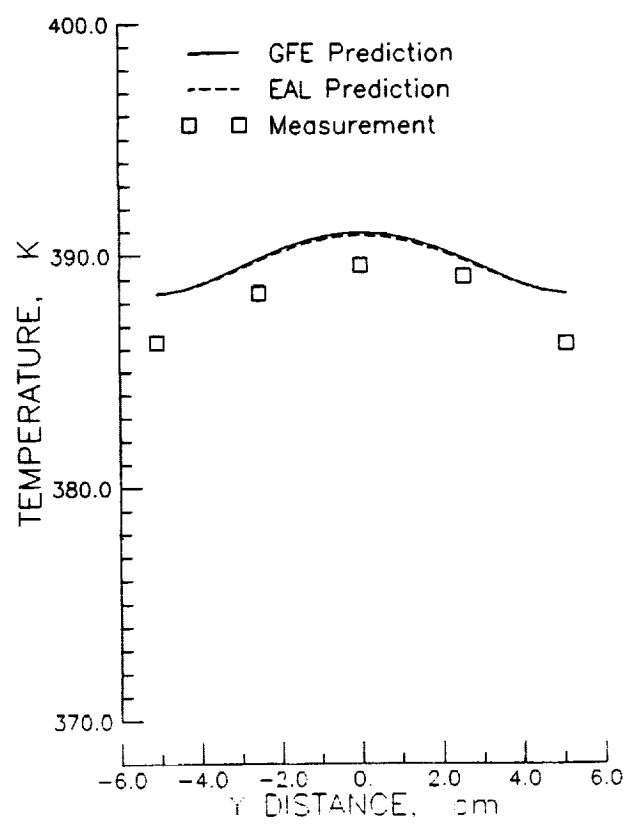

Figure 39.- Titanium specimen temperature distribution transverse to the axis of the lamp for a lamp-to-panel distance of 15.24 cm.

NASA National Aeronautics and Space Administration	Report Documentation Page		
1. Report No. NASA TM-101660	**2. Government Accession No.**	**3. Recipient's Catalog No.**	
4. Title and Subtitle Prediction of the Thermal Environment and Thermal Response of Simple Panels Exposed to Radiant Heat		**5. Report Date** October 1989	
		6. Performing Organization Code	
7. Author(s) Travis L. Turner Robert L. Ash		**8. Performing Organization Report No.**	
		10. Work Unit No. 506-80-31-02	
9. Performing Organization Name and Address NASA Langley Research Center Hampton, VA 23665-5225		**11. Contract or Grant No.**	
		13. Type of Report and Period Covered Technical Memorandum	
12. Sponsoring Agency Name and Address National Aeronautics and Space Administration Washington, DC 20546-0001			
		14. Sponsoring Agency Code	

15. Supplementary Notes

Travis L. Turner: Langley Research Center, Hampton, Virginia
Robert L. Ash: Old Dominion University, Norfolk, Virginia.

16. Abstract
A method of predicting the radiant heat flux distribution produced by a bank of tubular quartz heaters was applied to a radiant system consisting of a single unreflected lamp irradiating a flat metallic incident surface. In this manner, the method was experimentally verified for various radiant system parameter settings and used as a source of input for a finite element thermal analysis. Two finite element thermal analyses were applied to a thermal system consisting of a thin metallic panel exposed to radiant surface heating. A two-dimensional steady-state finite element thermal analysis algorthim, based on Galerkin's Method of Weighted Residuals (GFE), was formulated specifically for this problem and was used in comparison to the thermal analyzers of the Engineering Analysis Language (EAL). Both analyses allow conduction, convection, and radiation boundary conditions. Differences in the respective finite element formulation are discussed in terms of their accuracy and resulting comparison discrepancies. The thermal analyses are shown to perform well for the comparisons presented here with some important precautions about the various boundary condition models. A description of the experiment, corresponding analytical modelling, and resulting comparisons are presented.

17. Key Words (Suggested by Author(s)) heat transfer thermal testing thermal analysis finite elements radiant heat		**18. Distribution Statement** Unclassified - Unlimited Subject Category 71	
19. Security Classif. (of this report) Unclassified	**20. Security Classif. (of this page)** Unclassified	**21. No. of pages** 56	**22. Price** A04

NASA FORM 1626 OCT 86